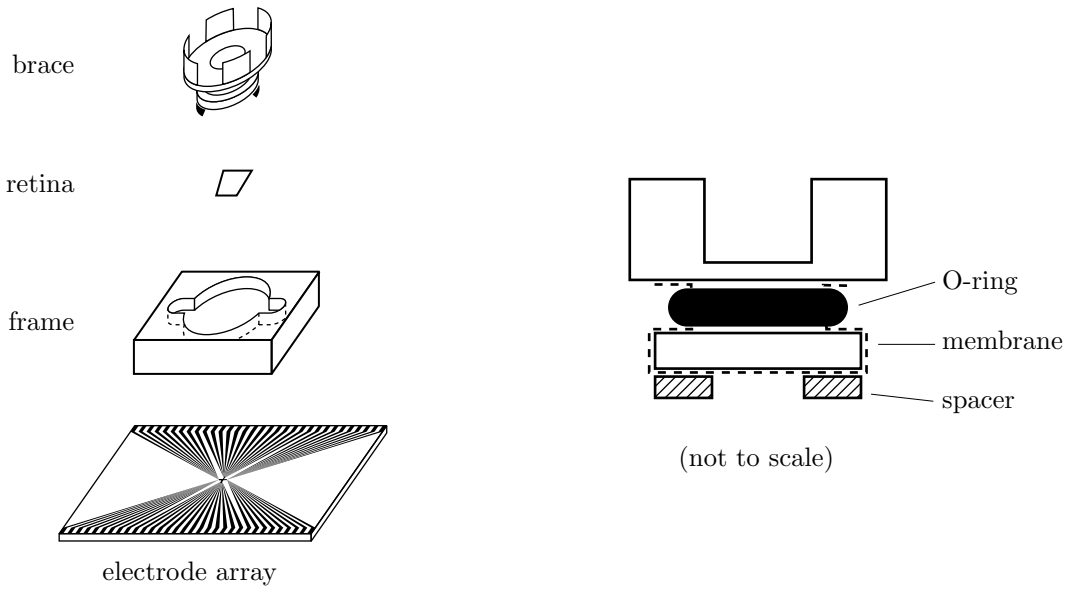

Figure 2.3: (a) Array assembly. During experiments the array, frame, retina and castle-shaped brace were vertically compacted. The frame was sealed to the array with RTV118 silicone (GE Silicones, Waterford, NY, USA) to provide a fluid-tight seal. The leaves at the top of the brace pressed tightly against the walls of the frame so that the bathing medium would not buoy it up off of the retina. (b) Detailed view of the brace.

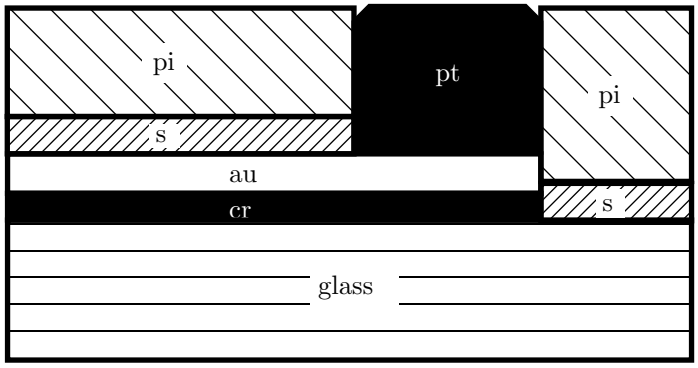

Figure 2.4: Cross-section view of the electrode array (not to scale). Abbreviations and layer thicknesses: cr=chrome, 650Å; au=gold, 5000Å; s=silicon nitride, 2000Å; pi=polyimide, 10μm; pt=platinum black, approximately 10μm.

2.3.1 Cross-section

A cross-section view of the electrode array is shown in Figure 2.4. The thin chrome layer acted as a glue between the gold and glass, which do not adhere well to one another. A combination of silicon nitride and polyimide were used as insulation. The silicon nitride provided an effective barrier to resistive current flow, while the thick polyimide layer reduced capacitance between the gold wires and solution. To reduce electrode impedances to approximately 100kΩ magnitude at 1kHz, the gold surfaces were coated with platinum black (Kovacs, 1994; Regehr et al., 1989). This was accomplished by immersing the electrodes in a dilute solution of chloroplatinic acid and lead acetate (YSI Inc., Yellow Springs, OH, USA) and driving -0.3μA through each 10μm-diameter electrode, using a platinum wire for the return, for approximately ten seconds. The same treatment was re-applied as needed if, for example, electrodes had a low signal-to-noise ratio when used for recording.

2.3.2 Electrode layout

The electrode array pattern used in this thesis is shown in Figure 2.2.The dark spots in the Figure are 10μm-diameter areas where the gold conductors were exposed and coated with platinum black. The polyimide and silicon nitride insulation layers, which are not visible in the image, cover the entire area except for the platinized electrodes.

The electrodes on the array were grouped into two clusters, one typically used for recording and the other for stimulation. The clusters were spaced several hundred microns apart to reduce stimulus artifacts, as discussed in Section 2.4.5. The electrodes in the recording cluster were arranged hexagonally on 70μm centers, as in other stud-

ies where similar recordings were made (Meister et al., 1994). The electrodes in the stimulating cluster were spaced more closely together, with 25μm center-to-center spacing, to allow for good resolution (i.e. on the order of the electrode diameter) when sampling thresholds versus position.

2.3.3 Electrical connections to instruments

The lighter lines in Figure 2.2 are chrome/gold wires which extended to the edges of the glass substrate and provided individual access to each electrode. Following preparation of the retina patch, the electrode access wires were brought into register with conducting traces on an adjacent printed circuit board. Voltages and currents were transmitted between the edges of the array and the printed circuit board through a Zebra Connector (Fujipoly America Corp., Kenilworth, NJ, USA). Conventional .025-inch square post connectors on the circuit board board provided access to the stimulator and nerve response amplifiers.

2.4 Data acquisition

The data acquisition system consisted of: (1) a voltage-controlled current source stimulator, with monitor amplifiers to measure the stimulus current and voltage; (2) an eight-channel nerve response amplifier, consisting of a pre-amplifier board located near the retina preparation and a rack-mounted high gain amplifier; (3) a Pentium computer with analog/digital interfaces; (4) a four-channel oscilloscope; (5) a speaker. The block-diagram in Figure 2.5 illustrates how these components were connected. The stimulator, monitor amplifiers and nerve response amplifiers were designed as part of the thesis. Circuit schematics and design considerations for these appear in Appendix B.

2.4.1 Multi-channel nerve response amplifier

The nerve response amplifier consisted of eight identical channels each with gain 10,000 and bandwidth 20-10,000Hz. The input to each amplifier was connected in parallel to eight electrodes through electro-mechanical relays, with only one relay in the closed position at a time. Channel inputs were selected using either pushbutton controls or software, allowing for easy monitoring of all sixty-four electrodes on the array during an experiment. Each channel measured the voltage of a single electrode relative to an earthed platinum wire at a distant location in the bathing medium. With the electrodes platinized and the retina patch mounted on the array, the noise floor for the amplifiers was typically 5-10μV rms.

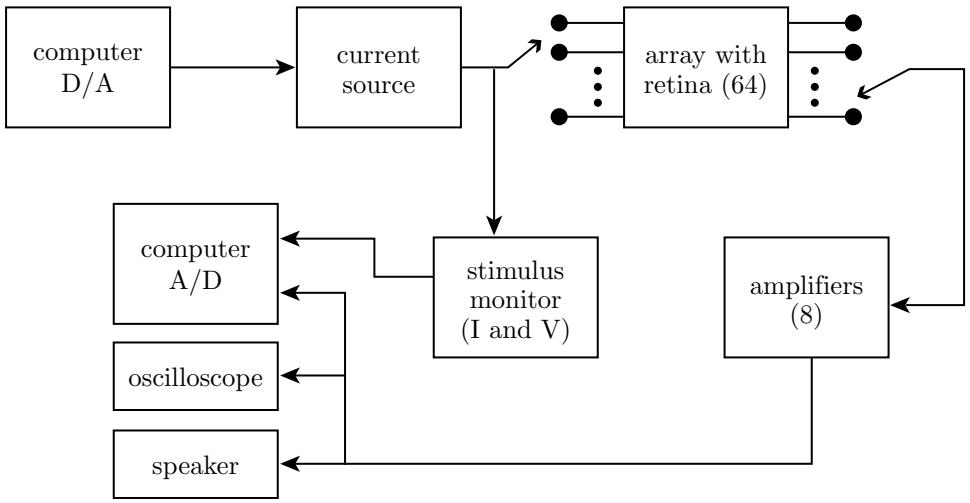

Figure 2.5: Block diagram of the data acquisition system.

2.4.2 Stimulator

The stimulator delivered a current proportional to its input voltage by 2μA/V. It was capable of delivering .01-20μA with .01μA minimum resolution, $\pm$3.5V compliance, and a 10-90% risetime of 10μs when driving electrodes. Monitor amplifiers, built on the same circuit board as the stimulator, measured the load current and voltage. The load current was determined by measuring the voltage across a 10kΩ resistor placed in series with the load.

After a number of experiments had been completed, a calibration test was performed wherein the stimulation current was measured by a second method independent of the current monitor circuit used in the experiments. With the same stimulator configuration used in the experiments, threshold-level stimulation pulses were delivered to a resistor load. The voltage across the resistor was then measured differentially using a Tektronix TAS475 oscilloscope, and the current calculated by dividing this voltage by the load resistance. The oscilloscope measurement matched that of the current monitor.

The stimulator and monitor amplifier circuits were optically isolated from earth potential, which was used as the reference voltage for amplifying nerve responses.

2.4.3 Computer interface

The computer interface was implemented on a Pentium computer running the Linux operating system. Analog and digital signals were accessed and controlled though

a PC-resident DAP3000a/212 input/output card (Microstar Laboratories, Bellevue, WA, USA). A 100kHz update rate was used for generating stimulus signals. For recording, 20kHz and 100kHz sampling rates were used for surveys of simultaneous activity at multiple sites and for threshold measurements at a single site, respectively.

A custom interface written in MATLAB was used to generate stimulation waveforms, display and analyze data, and control amplifier channel settings.

2.4.4 Oscilloscope and speakers

A four-channel oscilloscope and speaker provided additional means of monitoring nerve activity. The speaker was usually connected to a recording site with moderate spontaneous activity (see Section 2.5.1), which produced audible clicks above the baseline noise, and left on for the duration of an experiment. A steady stream of clicks over a period of hours was taken as a sign of good retinal health. The oscilloscope was used for measurements where the computer's re-plotting rate (approximately 1Hz using MATLAB's `plot()` command for eight 1000-point waveforms) was unacceptably slow. Examples included surveys of average discharge rates across the array and determinations of approximate excitation thresholds (see Section 2.5.2).

2.4.5 Reducing stimulus artifacts

A substantial effort, described further in Appendix C, was devoted to reducing stimulus artifacts. Two measures taken toward this end were particularly effective. These had the common aim of reducing coupling between the stimulating and recording instruments. First, the quality of the electrode insulation was improved by increasing the thickness of the polyimide layer from 1μm (used in early designs) to 10μm and by adding a silicon nitride layer (not present in early designs). These changes were motivated by the finding that stimulus artifacts were due in part to parasitic leakage between access wires for stimulating and recording electrodes. Compared with initial designs, the new arrays had less leakage between wires and smaller stimulus artifacts*. Second, the layout of the electrodes was modified from the original all-hexagonal arrangement (Meister et al., 1994; Regehr et al., 1989). To reduce coupling through tissue and parasitic current pathways, the electrodes were divided among two clusters spaced several hundred microns apart, with their access wires running to opposite edges of the array.

A number of conventional techniques were either found not to reduce the artifacts or were not fully exploited. A sample-and-hold circuit, for example, was placed between the preamplifier and high gain stage in all eight of the nerve response am-

*It has been suggested that the reductions in leakage and artifacts were due primarily to the addition of the silicon nitride layer, since polyimide may support ionic current flow (J. Pine – personal communication). An attempt has not been made to distinguish between contributions of thickening the polyimide and adding the silicon nitride.

plifiers, to prevent saturation and transients in high-pass filters. This circuit offered no consistent improvement. The preamplifiers did not typically saturate either, as verified by direct examination of their outputs. Hence the dominant artifact source was present at pre-amplifier inputs.

In addition, current sources and stimulus monitors were all optically isolated from the recording ground. The isolation was compromised, however, when making monopolar threshold measurements. For these measurements the negative terminal of the current source was connected to the recording ground, which served as the distant return. Stimulus artifacts in such cases were larger than for the bipolar stimulation configurations used in Chapter 3, but were still acceptable for a useful range of low-amplitude stimuli.

2.5 Physiologic recordings

2.5.1 Spontaneous and light-evoked activity

Varying amounts of nerve activity were discernible in the voltage signals at the response amplifier outputs, with spontaneous activity present on most recording sites. Spontaneously active sites produced signals consisting of a time series of discrete discharges, ranging in frequency from below one discharge/sec up to several tens of discharges/sec, superimposed on the baseline noise.

The discharges were judged to be single unit action potentials from ganglion cells (or possibly displaced, spiking amacrine cells), based on the following properties:

- **rates of spontaneous discharge** consistent with previous reports from rabbit retina (Ames III and Pollen, 1969; Caldwell and Daw, 1978; Ames III and Masland, 1976),
- **burst responses to changes in illumination** observed upon passing one's hand (darkening) or a flashlight beam (brightening) over the preparation,
- **discharge amplitudes** consistent with those obtained from salamander ganglion cells using a similar preparation (Meister et al., 1994), and
- **discharge waveforms** resembling those found in the cat retina (Kuffler, 1953).

The discharge waveforms, while somewhat variable, were well represented by the three types shown in Figure 2.6. The Type 1 discharges had a prominent initial negative deflection lasting 300-400μs, followed by a smaller, longer lasting positive deflection. Type 2 discharges had an initial positive deflection followed by a negative deflection, with a total duration comparable to that of the initial negative deflection of the Type 1 discharges. The Type 3 discharges had an initial positive-negative sequence like the Type 2 discharges, but also had a third, positive deflection.

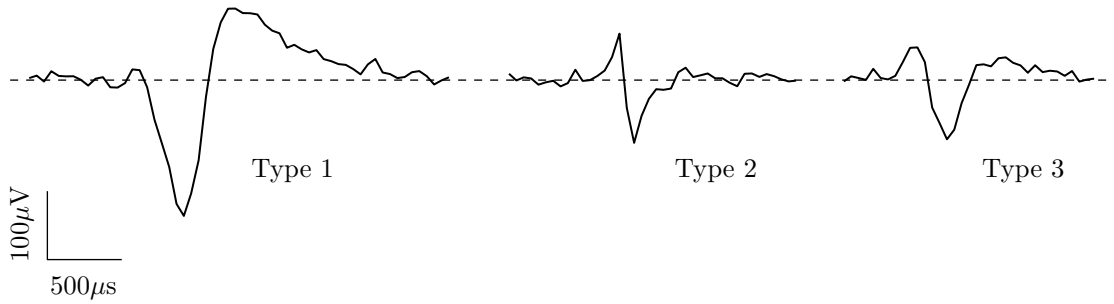

Figure 2.6: Examples of different spontaneous discharge types. Negative electrode voltages are plotted downward.

Correlated discharges on two or more electrodes, arising from pickup of the same unit, were common (Meister et al., 1994). These correlations often appeared on neighboring electrodes in the recording cluster, among all combinations of discharge types (i.e. Type i/Type j, where i, j=1,2,3). On the other hand, Type 2 discharges sometimes appeared in near simultaneity with discharges—of any type—on electrodes several hundred microns away. Furthermore, Type 2/Type 2 correlated discharges could be found on as many as four recording sites. These correlations always appeared on groups of electrodes roughly aligned with the expected optic nerve fiber direction. Closer inspection of the waveforms revealed a systematic ordering, with discharges appearing first on the recording sites furthest from the optic disk, and progressively later with decreasing distance from the disk. Apparent velocities, computed by dividing the distance between recoding sites by the time delay between negative peaks of the discharges, were 0.8-1.5m/s (n=13). These correlation properties, which were only seen for the Type 2 discharges, suggest that the Type 2 discharges were generated by ganglion cell axons, as discussed in Section 2.6.

It was also common to record numerous discharges of different types and amplitudes from a single electrode.

2.5.2 Electrically evoked activity

Properties of electrically evoked activity were studied by injecting current through stimulating electrodes while monitoring voltages in the recording cluster. All measurements in this chapter were made using a monopolar configuration, with the stimulator connected between a single stimulating electrode and the distant recording ground. Unless otherwise specified, stimuli were charge-balanced biphasic pulse pairs (anodic phase first) with 400μs phases and 400μs intra-phase delay, applied at a rate of 10/sec.

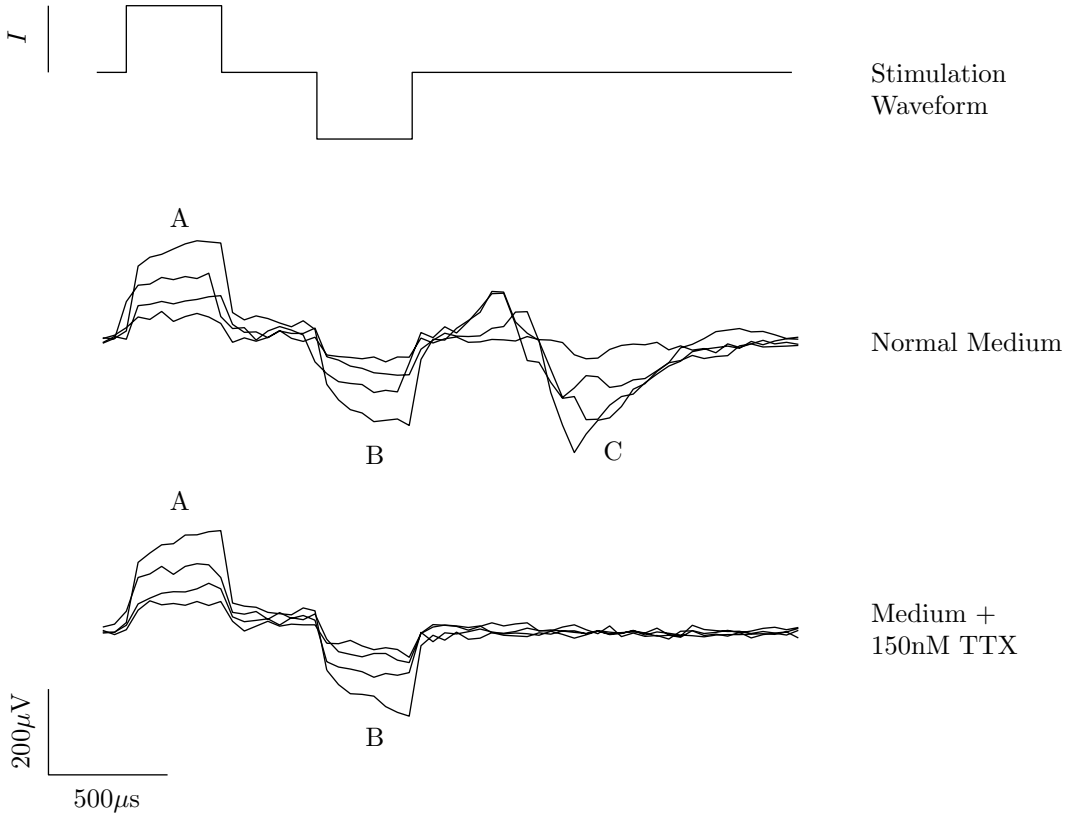

Figure 2.7: Overlay of response waveforms for four different stimulus amplitudes, before (middle traces) and after (bottom traces) addition of 150nM tetrodotoxin. The stimuli (top trace) were applied "by hand" at roughly fifteen second intervals. The amplitudes were $I = \pm.10$, $\pm.14$, $\pm.20$, and $\pm.29\mu$A.

Stimulus artifacts, graded potentials, and spikes

Figure 2.7 shows the most commonly observed responses to electric stimulation. In normal medium (middle traces), the responses had three components, labeled A, B, and C, which all grew with increasing stimulus amplitude. The A and B components were coincident with the positive and negative phases of the stimulus waveform (top trace), respectively, while component C arrived after the end of the stimulus. Addition of 150nM tetrodotoxin (TTX) abolished only the C component, as shown in the bottom traces. Hence the A and B components were stimulus artifacts while the C component was of neuronal origin.

It was also possible to record responses that, when they appeared, varied little with stimulus amplitude. This property is illustrated in Figure 2.8. Response compo-

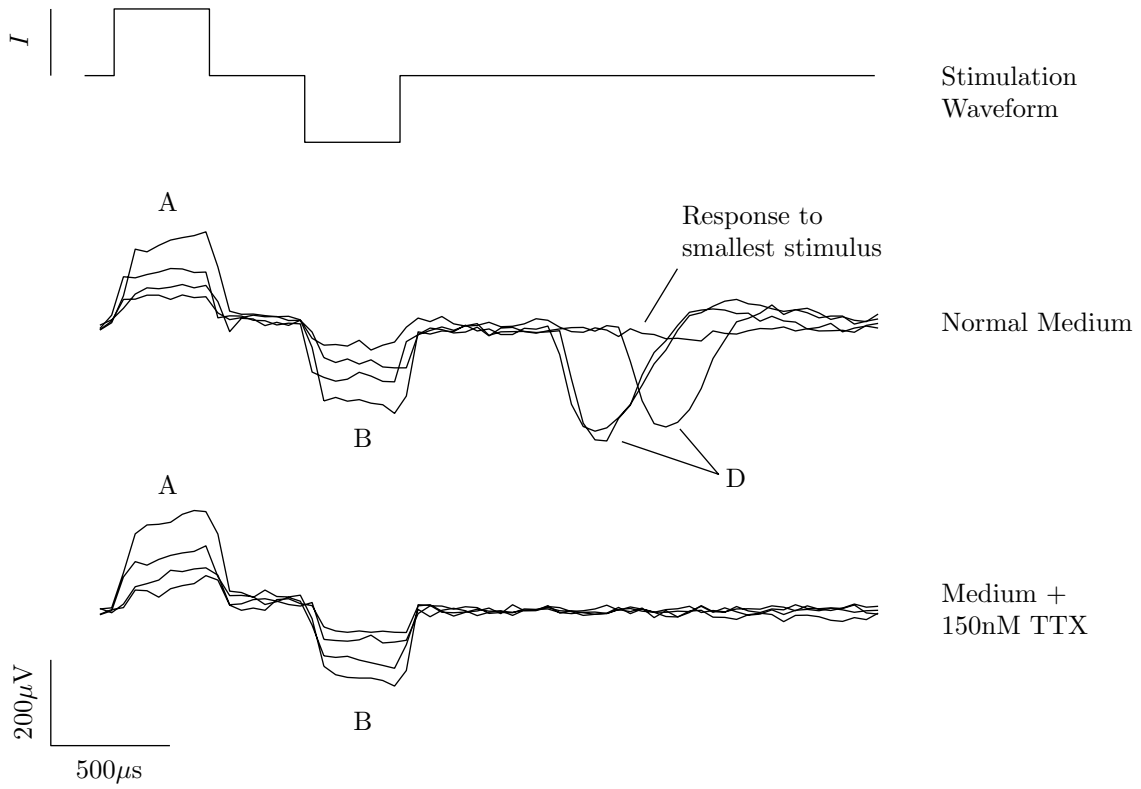

Figure 2.8: Response waveforms with an all-or-none component. Stimuli had the same timing and levels as in Figure 2.7.

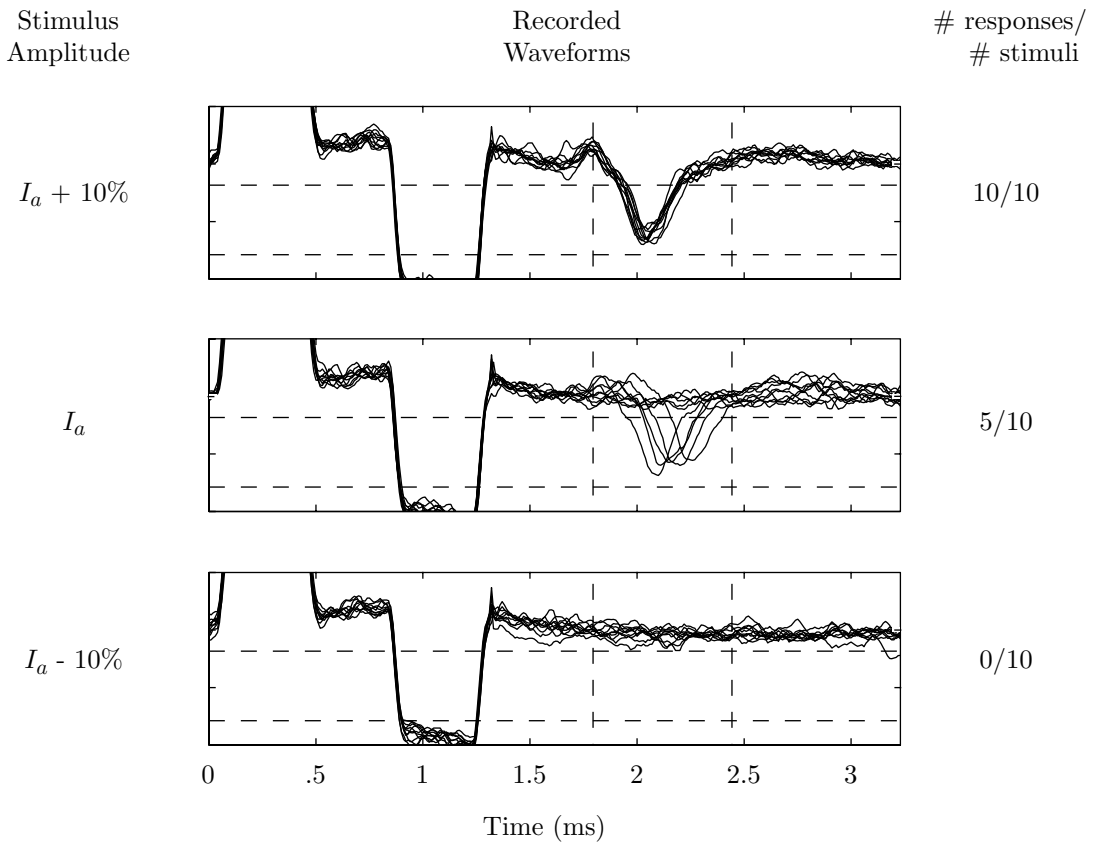

Figure 2.9: Example threshold measurement, with $I_a = .22\mu$A and the same stimulus timing as in Figure 2.7. Each waveform entering the region bounded by the dashed lines was counted as a response. Vertical ticks are at 100μV intervals.

nents A and B were stimulus artifacts as before. The D component failed to appear in response to the lowest amplitude stimulus and also after addition of 150nM TTX. While the latency of the D component was variable for the three largest stimuli, the response shape was highly conserved.

At specific threshold amplitudes the all-or-none responses appeared variably and with variable latencies. To measure thresholds precisely, an approximate threshold I_a was first determined by applying stimuli at a rate of 2-5/sec and manually varying the amplitude until the all-or-none response occurred roughly half the time. Next, the computer was used to present ten stimuli at each of three different amplitudes in a randomized order at 10/sec. Results from the automated measurement were plotted after presentation of all thirty stimuli. An example is illustrated in Figure 2.9. In this case the estimate I_a was equal to the threshold, defined as the amplitude at

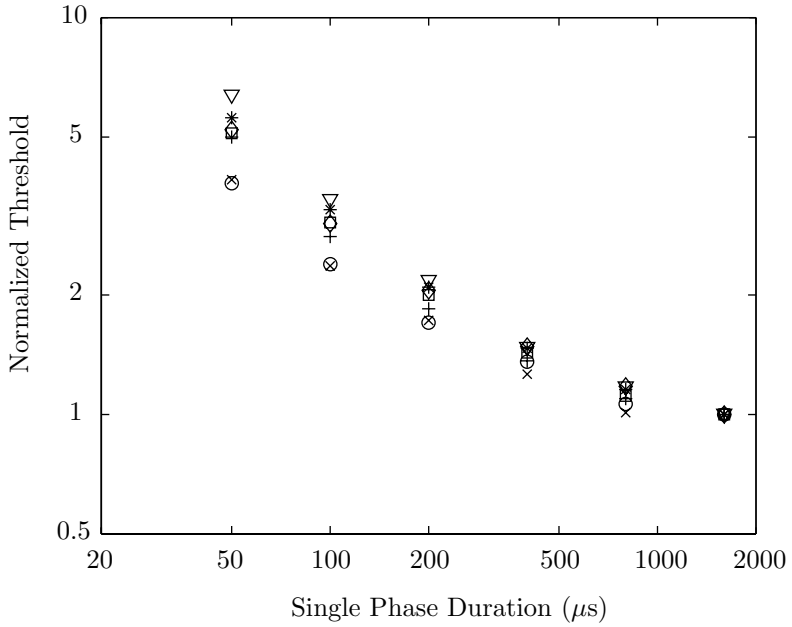

Figure 2.10: Normalized thresholds vs. phase duration for seven recording sites in seven retinas. Stimuli were anodic-first charge-balanced biphasic pulse pairs with equal phase durations and 400μs intra-phase delay. Thresholds at each recording site were normalized to the threshold for 1600μs phase duration. A unique symbol is used to plot measurements from each cell.

which responses occurred on half of the stimulus presentations. A relatively small deviation from I_a was sufficient to eliminate the variability: responses occurred on every presentation at ten percent above I_a and on no presentations at ten percent below I_a.

The thresholds for the all-or-none responses were dependent on the stimulus phase duration, as shown in Figure 2.10. Thresholds fell with increasing phase duration.

Responses were also refractory. This property was observed in several experiments, and measured carefully in one. The experiment utilized a pair of 400μs cathodal pulses, separated by a variable delay, as the stimulus. The first pulse was set to a supra-threshold amplitude, and the excitation threshold for the second pulse measured as a function of intra-pulse delay. Thresholds rose by 1.5 times as the delay between the two pulses was reduced from 4ms to 1ms.

Based on the all-or-none, duration-dependent, and refractory properties, as well as sensitivity to TTX, these responses were judged to be single unit spikes.

Additional properties of spike responses

While stimuli were almost always biphasic, the cathodic phase of the stimulus was most effective for generating spikes. The roles of the anodic and cathodic phases in spike generation were investigated by applying anodic-first and cathodic-first stimuli to the same unit. As exemplified in Figure 2.11, spike responses tracked the cathodic phase of the stimulus. The spikes were generated by the cathodic phase, and hence cathodic thresholds were lower than anodic thresholds. Furthermore, thresholds were the same for anodic-first and cathodic-first stimuli for a 400μs intra-phase delay. Anodic-first stimuli were used in order to minimize contamination of the response signal by the stimulus artifact.

A number of additional properties were characterized to support the claim (see Section 2.6) that responses were due to direct stimulation of ganglion cell axons. Two properties suggested that stimulation was direct rather than trans-synaptic. First, as suggested by the tests for refractoriness, spikes could be generated at high repetition rates. An example is illustrated in Figure 2.12, where responses were produced at approximately 2ms intervals. Second, spike responses were robust to addition of 200μM cadmium (a synaptic blocker) to the bathing medium. During fifteen minute period following start of cadmium flow, thresholds fluctuated but remained close to (within 30% of) pre-cadmium values. By contrast, responses to light were eliminated within minutes of the introduction of cadmium.

In a third type of measurement, thresholds were determined at numerous locations in the stimulating electrode cluster to produce a rough map of the target. Threshold variations with distance were different for the horizontal and vertical directions on the stimulating grid, as shown in the map of Figure 2.13.

The lowest thresholds on the map occurred along a vertical line, presumably closest to site(s) of excitation, with thresholds rising to the left and right. While the thresholds varied with vertical distance in the left and right columns, the threshold change per unit distance was at least a factor of two smaller than variations in the horizontal direction. Hence the target had an elongated, nearly vertically aligned geometry. This pattern of threshold changes was consistent across a number of experiments which will be described in Chapter 3.

Additional notes on threshold measurements

Dashed lines like the ones in Figure 2.9 were used to define a range of amplitudes and a segment of time that were used as a criteria for discriminating all-or-none responses from other signal components such as stimulus artifacts and discharges from other neurons. The line positions, which could be altered as needed during an experiment, were always identical in the response plots for the three different stimulus amplitudes used for each threshold measurement (see Figure 2.9). The tallies on the right side of the Figure were computed by counting only response waveforms with ten or more sample points ($\geq$100μs total duration) in the region bounded by the four lines.

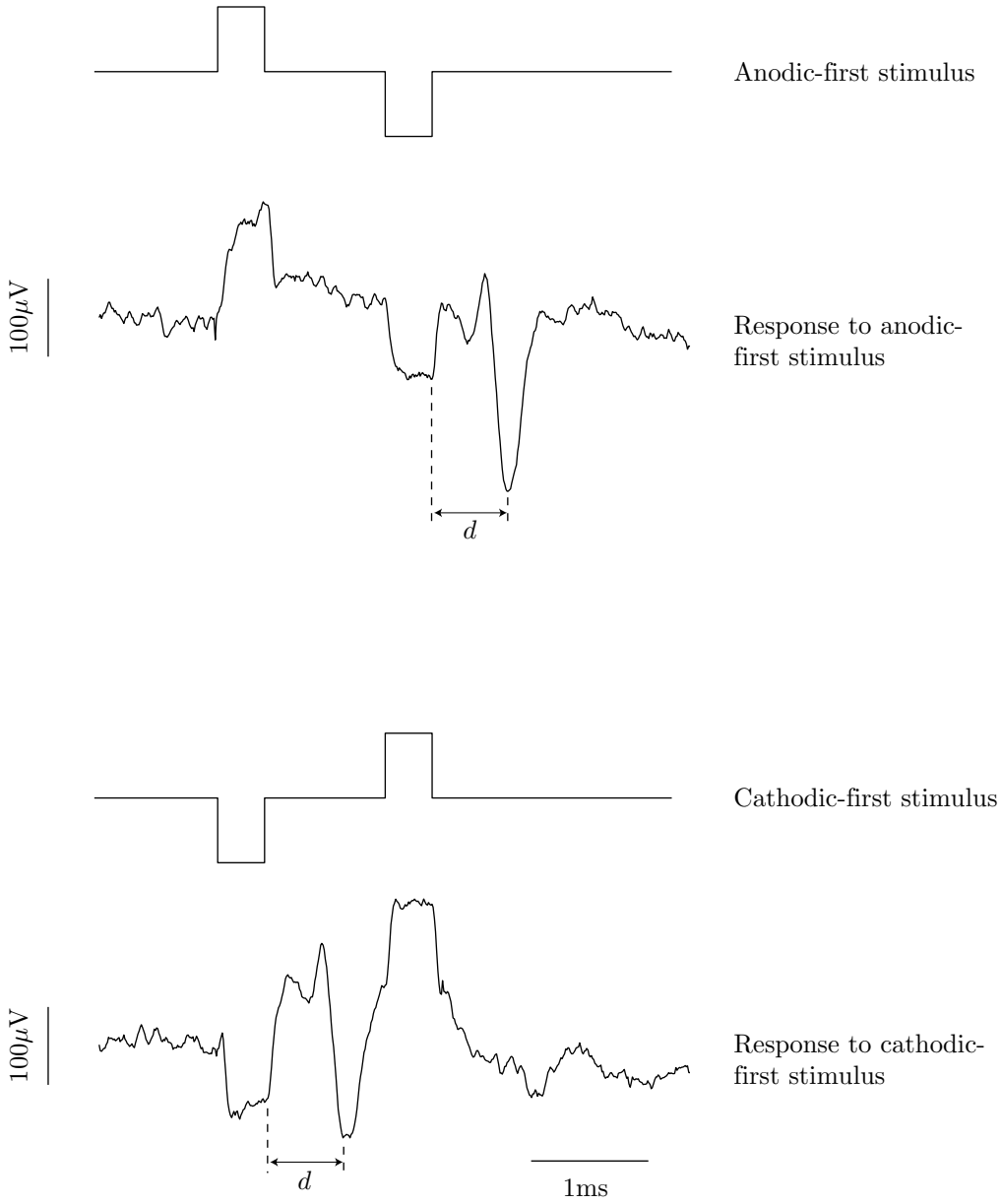

Figure 2.11: Stimulus and response waveforms for anodic-first and cathodic-first stimulation. The interval from the end of the cathodic phase to the negative peak of the spike, indicated by the horizontal lines below each waveform, was equal for the two cases ($d = 620\mu$s). An unusually long intra-phase delay of about 1ms was used to minimize contamination of the response by the artifact accompanying the anodic phase of the cathodic-first stimulus. The stimulus level was .17μA.

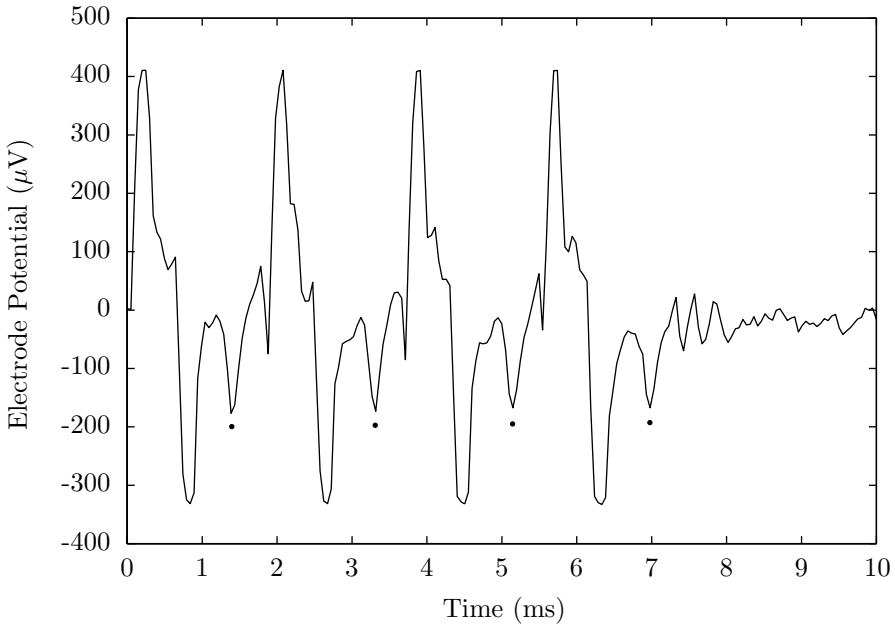

Figure 2.12: Responses to repetitive supra-threshold stimulation at approximately 500 stimuli/sec. Spikes are indicated by the dots below them.

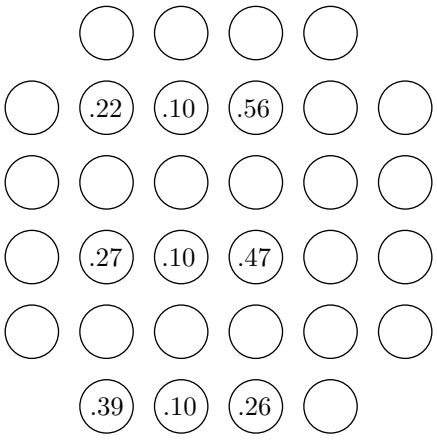

Figure 2.13: Map of thresholds for a single unit, measured by connecting the stimulator to nine different electrodes in the stimulating electrode cluster, one electrode at a time. Thresholds are in μA.

Since the recording electrodes often picked up discharges from multiple neurons, the shape of an all-or-none spike was stored at the beginning of a series of measurements. The stored spike was then displayed on the computer screen in a contrasting color while additional responses were measured. A series of responses—measured against variations in some stimulation parameter—was only attributed to one cell if these responses could be distinguished from other signal components and if they resembled the template.

The initial threshold estimate I_a was not always exact as in Figure 2.9. In cases where less than five responses were generated at one of the stimulus amplitudes and more than five responses were generated at a larger amplitude, thresholds were estimated by linear interpolation.

Control measurements, taken under nominally the same conditions as an earlier measurement, were often made during the course of an experiment. These usually fell within $\pm 10\%$ of the initial measurement. Out of 25 repeat measurements from eight cells, for example, 19 of these were within $\pm 10\%$ of the initial measurement and all were within $\pm 26\%$.

2.6 Discussion

This chapter has described a method for electrically stimulating and recording from retinal neurons using a multi-electrode array, and illustrated basic properties of the responses thereby obtained. One of the primary strengths of this method was illustrated in the example map of Figure 2.13, where excitation thresholds for a large number of electrode configurations were rapidly measured without any mechanical disruption of the retina preparation. This capability will be further exploited in Chapter 3. A second strength of this method is the great flexibility it affords in the design of stimulating electrode geometries. Further application of this advantage to the optimization of stimulation parameters for an epi-retinal prosthesis will be the focus of future work, as discussed in Chapter 5.

The arrangement of electrodes and orientation of the retina on the array were chosen to facilitate the study of excitation thresholds for ganglion cell axons. Several lines of evidence weigh against other stimulation sites such as pre-synaptic neurons or somata. Two different results discount the possibility of trans-synaptic stimulation. First, the responses remained in the presence of the synaptic blocker cadmium, at a concentration which eliminated responses to light and which completely blocked excitatory inputs to salamander ganglion cells (Mittman et al., 1990)[†]. Second, the spikes could be produced repetitively at intervals comparable to those required for synaptic transmission.

[†]A much larger concentration of 2mM cadmium chloride has been used in some amphibian experiments(Greenberg, 1998a; Grumet et al., 1998). This concentration was unusable in Ames' medium, which is commonly used for rabbits but for not amphibians, due to the formation of precipitate at physiologic pH.

Additional considerations show that the possibility of soma stimulation is unlikely. Spike responses were recorded at sites 300-700μm more distant from the optic disk than the stimulating electrodes. Were excitation initiated in nearby somata, the largest of which are perhaps 30μm in diameter (Amthor et al., 1983; Peichl et al., 1987), the responses could only have been recorded from axons or dendrites. Neither of these possibilities is likely, however, since axons course toward the optic disk upon emerging from somata and because dendrites, owing to their small caliber and large distance from the retinal surface, make them poor targets for recording with a planar electrodes. In addition, threshold variations with distance were strongly direction-dependent, in one case remaining constant despite a 100μm electrode displacement along the expected axon direction (middle column of Figure 2.13). Thus the target had an elongated geometry and was aligned with the expected axon direction.

The above arguments do not rule out the possibility that dendrites were stimulated in addition to, or instead of, axons. In some ganglion cell types these can extend many hundreds of microns from somata (Amthor et al., 1983; Peichl et al., 1987), which would be just sufficient to span the distance between the stimulating and recording clusters on the electrode array (see Figure 2.2). Furthermore, antidromic propagation of action potentials in the dendrites of retinal ganglion cells has recently been demonstrated (Velte and Masland, 1999). Hence it is conceivable that the spike responses were initiated in dendrites. This possibility will be given further consideration in Section 3.5.4.

Reports of direct stimulation of ganglion cell axons and dendrites are rare in the literature on electrical stimulation of retina (see Section 1.2 for a review). In most cases the lowest threshold stimuli acted directly on photoreceptors or bipolar cells. The present results are not in conflict with these reports because focal responses—such as would be expected for photoreceptor or bipolar cell stimulation—would probably not be found on electrodes in the distant recording cluster. In fact, spike responses were commonly observed on electrodes within the stimulating cluster, though these were not carefully studied.

The anatomical origin of the response signals deserves consideration. There is some evidence that the sources of the all-or-none responses can be deduced from the spike shapes. These responses strongly resembled the spontaneous discharge types of Figure 2.6, most commonly Type 1 or Type 3. Consider first the Type 2 spontaneous discharges, which were almost certainly recorded from ganglion axons. These had diphasic, initially positive shapes similar to those predicted by biophysical models for fibers (Plonsey, 1969; Woodbury, 1960), and were observed propagating toward the optic disk with velocities comparable to those of cat ganglion cell axons (Stanford, 1987). Furthermore, the light responses of spikes with similar shapes were described in detail by Kuffler in his studies of cat retina (Kuffler, 1953). Since they could be recorded at various displacements from the unit's optic receptive field, Kuffler attributed these spikes to axons. Kuffler also recorded spikes resembling the initially negative Type 1 discharges, attributing them to somata since they were always

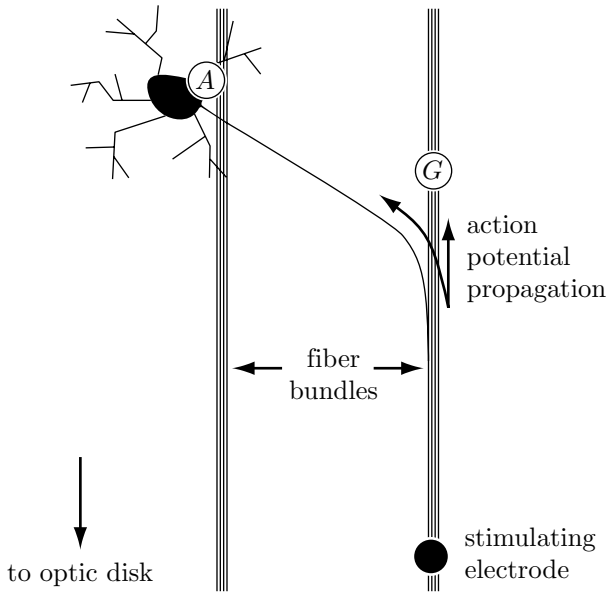

Figure 2.14: Speculative drawing of the anatomy underlying graded and all-or-none responses. A : Recording electrode with all-or-none response; G : recording electrode with graded response.

recorded within the optic receptive field (Kuffler, 1953). Hence the responses resembling Type 1 were probably due to nearby somata. The origin of the responses resembling Type 3 spontaneous discharges is less clear. Though their tri-phasic shape was also consistent with biophysical models for fibers, spontaneous Type 3 discharges were never seen propagating toward the optic disk.

The frequently observed graded responses were most likely compound action potentials in groups of ganglion cell axons, which gather into bundles as they course toward the optic disk (Peichl et al., 1987; Vaney, 1980). It is curious in light of this arrangement that the planar recording electrodes, which were large compared with conventional sharp-ended electrode tips, could isolate single unit responses at all. A clue to this dilemma comes from the observation that ganglion cell axons sometimes emerge from somata at oblique angles, crossing over one or more fiber bundles before joining one (Peichl et al., 1987). This situation is illustrated in Figure 2.14. An all-or-none response is picked up by the A recording electrode because the adjacent soma extends its axon near the stimulating electrode. Even though a fiber bundle also passes by this recording electrode, no graded responses are seen because this bundle is far from the stimulating electrode.

The scheme of Figure 2.14 also suggests that graded potentials might arise on

the A recording electrode for some stimulating electrode positions, even though all-or-none responses could be generated at others. In fact, this phenomenon was often observed in the threshold versus displacement experiments of Chapter 3.

Chapter 3

A Study of Fiber Excitation Thresholds Using Monopolar and Bipolar Stimulating Electrodes

3.1 Introduction

This chapter takes an experimental look at the problem of how to raise thresholds for stimulating axons. The experiments were motivated by reports that the excitability of elongated structures, such as axons or muscle cells, depended strongly on the orientation of the imposed electric field relative to the long axis of the structure. Thresholds were low with the stimulating field oriented along a structure and were high with the field oriented across the structure (Ranck, 1975; Ranjan and Thakor, 1995; Rushton, 1927; Tung et al., 1991). Analytical models employing infinite parallel plate stimulating electrodes and linear passive fibers predict transmembrane potential changes in accordance with this trend. In the steady state, longitudinal fields produce larger depolarizations than transverse fields provided that the plate separation is larger than a fiber diameter (Grumet, 1994; Plonsey and Altman, 1988).

These trends led my research group to hypothesize that axon thresholds could be raised with electrodes that minimize the longitudinal component of the stimulating field (Grumet, 1994; Wyatt and Rizzo, 1996). Experimental tests of this hypothesis were conducted using the apparatus described in Chapter 2, with the stimulator connected between electrode pairs oriented along or across target fibers (ganglion cell axons and possibly dendrites—see Sections 2.6 and 3.5.4) on the surface of the rabbit retina.

In addition, thresholds for monopolar stimulation (with distant return) of each fiber were measured at numerous sites in the stimulating electrode cluster. These were used to estimate the fiber locations, which provided a common reference frame for aggregating threshold data. A rough estimate of fiber locations could be made simply by inspection of threshold maps like the one in Figure 2.13. To illustrate,

the minimum threshold in that map (.1μA) appeared on three electrodes in the third column from the left. Hence the fiber was roughly aligned with this column. The fiber was probably not perfectly vertical, however, because the thresholds in the second and fourth columns varied along the vertical dimension. The thresholds in the second column decreased from .39μA to .22μA with increasing height in the column, whereas the thresholds in the fourth column increased from .26μA to .56μA. These variations were consistent with a fiber orientation which was rotated slightly counter-clockwise from vertical.

The fiber location estimates were formalized using two different mathematical models for thresholds as a function of distance to the monopolar stimulating electrode. The first model is derived from first principles. The second model is an empirical model. Predictions for bipolar thresholds were also developed for each model. The models are presented in the following section, and their application to location estimates is explained in Sections 3.3.2 and 3.6.

3.2 Models

3.2.1 First principles model

Activating function

A number of simplifying assumptions are made to model threshold variations with electrode position and orientation. The first is that axons satisfy the assumptions of the core conductor model. This general model underlies the cable and Hodgkin-Huxley models, but makes no assumptions regarding the electrical properties of the membrane. We will make use of the following core conductor equations (Weiss, 1996),

$$\frac{\partial I_i(z,t)}{\partial z} = -K_m(z,t),$$

$$\frac{\partial V_i(z,t)}{\partial z} = -r_i I_i(z,t),$$

$$V_m(z,t) = V_i(z,t) - V_o(z,t),$$

where z measures distance along the fiber, t is time, I_i is the axial current flowing in the fiber, K_m is the membrane current per unit length, V_i is the intracellular potential, r_i is the intracellular resistance per unit length, V_m is the membrane potential, and V_o is the potential on the outer surface of the membrane. These equations can be manipulated to yield

$$-\frac{\partial^2 V_m(z,t)}{\partial z^2} + r_i K_m(z,t) = \frac{\partial^2 V_o(z,t)}{\partial z^2} \tag{3.1}$$

which relates the membrane potential and current to the extracellular potential. The relation shows that the effective drive term for the membrane current and potential is the second spatial derivative of the extracellular potential in the longitudinal direction,

$$f_a = \frac{\partial^2 V_o(z,t)}{\partial z^2}.$$

This "activating function" f_a provides a useful tool for predicting fiber responses under a variety of stimulation conditions (Rattay, 1986). From equation 3.1, a positive activating function results in either an outward membrane current, a concave-downward membrane potential versus position, or both. The net result is to locally raise or depolarize the membrane potential. By a similar argument, a negative activating function tends to hyperpolarize the membrane. Thus the activating function may be taken as a rough picture of the membrane potential changes induced in a fiber by an extracellular stimulus.

Activating functions for stimuli used here may be derived if the following additional assumptions are made: 1) the tissue may be modeled as a uniform, linear conductor; 2) the presence of the fiber may be ignored when calculating the potential distribution during stimulation; 3) the planar, ten micron diameter electrodes may be modeled as point sources.

To calculate the activating function for a point source, we begin by finding the voltage it generates along a fiber. Consider a fiber oriented in the z-direction and a point source in the $z = 0$ plane, as illustrated in Figure 3.1a. The potential at points along the fiber is given by

$$V_o = \frac{i}{4\pi\sigma}(z^2 + D^2)^{-1/2},$$

where i is the stimulating current, σ is the conductivity of the medium, D is the minimum distance between the point source and fiber.

Carrying out the derivatives yields the activating function,

$$f_a = \frac{i}{4\pi\sigma}(z^2 + D^2)^{-5/2}(2z^2 - D^2).$$

Figure 3.1b illustrates the shape of the curves for cathodal stimuli ($i < 0$) located at $D = 1, 1.5$ and 3. The plots are consistent with two expected outcomes. First, the activating function is maximal, or most strongly depolarizing, at the point along the fiber which is closest to the cathode ($z = 0$). Second, the maximal value decreases with increasing distance between electrode and fiber.

Thresholds for monopolar stimulation

These observations suggest a simple way to model the threshold increase accompanying electrode movement away from the fiber. Consider the activating function's

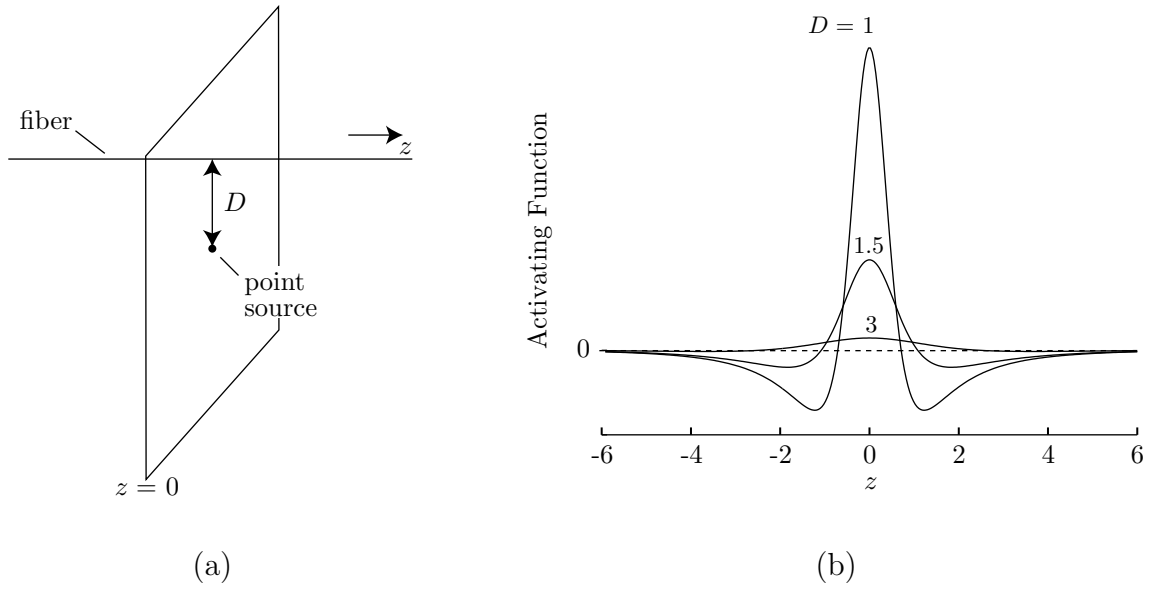

Figure 3.1: Activating functions for a point source electrode. (a) Point source in the $z = 0$ plane, at a distance D from the fiber. (b) Activating functions for cathodal stimuli at $D = 1, 1.5, 3$.

maximum, at $z = 0$, for a threshold stimulus $i = -I_{thr}$ with the point source at a specific distance D_o,

$$f_a|_{\max,\text{thr}} = \frac{I_{thr}(D_o)}{4\pi\sigma} D_o^{-3}.$$

Now, if it can be assumed that the threshold value of f_a is independent of distance, we have

$$I_{thr}(D) = kD^3, \tag{3.2}$$

where

$$k = (4\pi\sigma)\ f_a|_{\max,\text{thr}}\,.$$

Equation 3.2 predicts the shape of the threshold versus position curve for a monopolar point source electrode. This equation can be viewed as the product of two factors, one describing spatial properties of the stimulus (D^3) and one containing information about the tissue and fiber (k).

Bipolar thresholds: along orientation

The approach which yielded equation 3.2 is readily applied to the bipolar stimulation case. For simplicity we will assume that the fibers are oriented exactly parallel or perpendicular to the bipolar electrode pair.

(a) (b)

Figure 3.2: Bipolar stimulation (a) along fiber and (b) across fiber using a pair of point sources separated by a distance d. *Abbreviations:* a=anode; c=cathode.

Figure 3.2a illustrates the case where a bipolar electrode pair is oriented along a fiber. The cathode c is located at $z = 0$ and the anode a is located at $z = d$. The fiber is at a lateral displacement x_o from the electrodes and at a height h. The activating function for the bipolar pair is

$$f_a = \frac{|i|}{4\pi\sigma}\{ \quad [x_o^2 + h^2 + (z-d)^2]^{-5/2}[2(z-d)^2 - x_o^2 - h^2] - \\ (x_o^2 + h^2 + z^2)^{-5/2}(2z^2 - x_o^2 - h^2) \ \}.$$

The shape of this function can be obtained by taking one of the curves in Figure 3.1b and subtracting a shifted version of itself. To a good approximation, the maximum value aligns with the cathode at $z = 0$, as before. Hence the threshold is given approximately by

$$I_{thr} = \frac{k}{(x_o^2 + h^2 + d^2)^{-5/2}(2d^2 - x_o^2 - h^2) + (x_o^2 + h^2)^{-3/2}}. \tag{3.3}$$

Bipolar thresholds: across orientation

Figure 3.2b illustrates the case where a bipolar electrode is oriented across the fiber. Both anode and cathode are located at $z = 0$. The fiber is at a height h above the point sources, and is laterally situated between cathode and anode. The lateral distance to the cathode is x_o, and the lateral distance to the anode is $d - x_o$. The activating function for the bipolar pair is

$$f_a = \frac{|i|}{4\pi\sigma}\{ \quad [(d-x_o)^2 + h^2 + z^2]^{-5/2}[2z^2 - (d-x_o)^2 - h^2] - \\ (x_o^2 + h^2 + z^2)^{-5/2}(2z^2 - x_o^2 - h^2) \ \}.$$

The shape of this function can be obtained by taking one of the curves in Figure 3.1b and subtracting a scaled version of itself. If we assume the cathode is closer to the fiber than the anode (consistent with the experiments described in the sections to follow) the maximum value aligns with the cathode at $z = 0$ and the threshold is given by

$$I_{thr}(x,h) = \frac{k}{(x_o^2+h^2)^{-3/2} - [(d-x_o)^2+h^2]^{-3/2}}. \tag{3.4}$$

3.2.2 Empirical model

In numerous experiments reported in the literature, the relationship between threshold and distance was well-described by

$$I_{thr} = \hat{k}D^2 + I_{min} \tag{3.5}$$

where I_{thr} is the excitation threshold, $\hat{k}$ is a constant having different units than k above, D is the distance between the electrode and target, and I_{min} is the minimum threshold (Tehovnik, 1996). Note that I_{min} is effectively zero for the first principles model since the activating function for a point source becomes infinite at zero distance.

Extension of this model to the bipolar case is less straightforward than for the first principles model. One plausible approach is suggested by the fact that in an unbounded, uniform linear medium the electric field magnitude for a point source of current is

$$|\mathbf{E}| = \frac{|i|}{4\pi\sigma r^2}$$

where $\mathbf{E}$ is the electric field and r is the distance from the source. If D is defined as the minimum distance between the point source and a fiber, the maximum electric field magnitude experienced by the fiber is

$$|\mathbf{E}|_{max} = \frac{|i|}{4\pi\sigma D^2}$$

assuming that the field at the fiber is not modified by the presence of the fiber. Consider this maximum for a threshold stimulus $i = -I_{thr}$ with the point source at a specific distance D_o,

$$|\mathbf{E}|_{max,thr} = \frac{I_{thr}}{4\pi\sigma D_o^2}.$$

If it can be assumed that the threshold value of $|\mathbf{E}|$ is independent of distance, then

$$I_{thr} = \hat{k}D^2 \tag{3.6}$$

where

$$\hat{k} = (4\pi\sigma)|\mathbf{E}|_{\mathrm{max,thr}}.$$

This result is equivalent to equation 3.5 provided that I_{min} is zero.

Bipolar thresholds: along orientation

If the cathode in Figure 3.2a is located at the origin, the normalized electric field components generated by the bipolar electrode pair at points $(x = x_o, y = h, z)$ along the fiber are given by

$$\begin{aligned}
\overline{\mathrm{E}}_x &= x_o \left\{ (x_o^2 + h^2 + z^2)^{-\frac{3}{2}} - \left[x_o^2 + h^2 + (z-d)^2 \right]^{-\frac{3}{2}} \right\}, \\
\overline{\mathrm{E}}_y &= h \left\{ (x_o^2 + h^2 + z^2)^{-\frac{3}{2}} - \left[x_o^2 + h^2 + (z-d)^2 \right]^{-\frac{3}{2}} \right\}, \\
\overline{\mathrm{E}}_z &= z(x_o^2 + h^2 + z^2)^{-\frac{3}{2}} - (z-d) \left[x_o^2 + h^2 + (z-d)^2 \right]^{-\frac{3}{2}}
\end{aligned}$$

where normalization was accomplished by dividing each field component by $i/4\pi\sigma$. The magnitude of the normalized field is computed from

$$|\overline{\mathbf{E}}| = \sqrt{(\overline{\mathrm{E}}_x)^2 + (\overline{\mathrm{E}}_y)^2 + (\overline{\mathrm{E}}_z)^2}.$$

The maximum magnitude, which occurs at $z = 0$ (and also at $z = d$), can be readily calculated for specified x_o, h, and d. As in the monopolar case, the predicted threshold is proportional to the reciprocal of this maximum value,

$$I_{thr} = \frac{\hat{k}}{|\mathbf{E}|_{max}(x_o, h, d)}. \tag{3.7}$$

Bipolar thresholds: across orientation

If the cathode in Figure 3.2b is located at the origin and the anode is located at $(x = d, y = 0, z = 0)$, the normalized electric field components generated at points $(x = x_o, y = h, z)$ along the fiber are given by

$$\begin{aligned}
\overline{\mathrm{E}}_x &= \left\{ x_o(x_o^2 + h^2 + z^2)^{-\frac{3}{2}} - (x_o - d) \left[(x_o - d)^2 + h^2 + z^2 \right])^{-\frac{3}{2}} \right\}, \\
\overline{\mathrm{E}}_y &= h \left\{ (x_o^2 + h^2 + z^2)^{-\frac{3}{2}} - \left[(x_o - d)^2 + h^2 + z^2 \right]^{-\frac{3}{2}} \right\}, \\
\overline{\mathrm{E}}_z &= z \left\{ (x_o^2 + h^2 + z^2)^{-\frac{3}{2}} - \left[(x_o - d)^2 + h^2 + z^2 \right]^{-\frac{3}{2}} \right\}.
\end{aligned}$$

The maximum magnitude, which occurs at $z = 0$, can be readily calculated for specified x_o, h, and d. The predicted threshold is proportional to the reciprocal of this maximum value.

3.3 Methods

3.3.1 Threshold measurements

The methods for isolating rabbit retinas, sustaining them *in vitro*, and recording responses from their neurons to electric stimulation are described in Chapter 2. All

threshold measurements used the same charge-balanced, four hundred microsecond per phase rectangular stimulus with a four hundred microsecond delay between phases (also shown in Figure 3.3d).

After mounting the retina in its chamber, a search was performed to find a recording electrode which exhibited all-or-none responses to stimulation through one of the stimulating electrodes. A platinum wire at the edge of the bath served as both the current source return and the recording ground. Responses were monitored on eight electrodes at a time as the amplitude of the stimulus waveform was varied from zero to approximately $\pm.3\mu$A. Compound responses, which grew in proportion to the stimulus, were picked up on the majority of the electrodes. When an all-or-none response was found, the excitation threshold was measured and the response shape stored for comparison with subsequent measurements. This provided a check against attributing responses of two or more cells to a single cell, as discussed in Chapter 2.

Next a threshold map was created from which the fiber's lateral displacement within the stimulating grid and tilt angle relative to vertical could be deduced. This was done by measuring a series of monopolar thresholds using adjacent electrodes along several rows of the stimulating grid, progressing along each row until a point of minimum threshold was found. One such map is shown in Figure 2.13. The number and distribution of threshold measurements in the map, a total of nine along three rows, was typical. Complete maps employing all thirty-two electrodes were not made primarily because stimulus artifacts often overtook the response signals as thresholds grew at large distances from the electrodes yielding lowest thresholds. Also, threshold measurements in additional rows (made on a few occasions) did not substantially alter the fiber position estimates.

Mapping efforts were often unsuccessful due to the appearance of responses from units other than the one initially identified. A recording electrode might pick up all-or-none responses to stimulation through some stimulating electrodes and graded responses to stimulation through others, as discussed at the end of Chapter 2. The distortion contributed by the firing of additional cells often made it impossible to accurately determine the threshold for the cell of interest. The search and mapping process was repeated until a recording electrode was found for which a complete map could be successfully produced. A map was considered complete when a single local minimum could be found in each row for two or more rows.

Once a map was successfully completed, thresholds were measured with the current source connected in different bipolar configurations on the stimulating grid. Bipolar electrode pairs were oriented either along or across the fiber as illustrated in Figure 3.3a and b, respectively. These measurements were always made in pairs. In each pair, the positive current source terminal, indicated by a + in Figure 3.3c, was held fixed. The orientation of the bipolar electrode pair was then controlled by switching the negative terminal (–) between either of two return electrodes. Hence a total of three electrodes was used for each pair of measurements. These electrodes usually had unequal monopolar thresholds, presumably due to unequal electrode-fiber

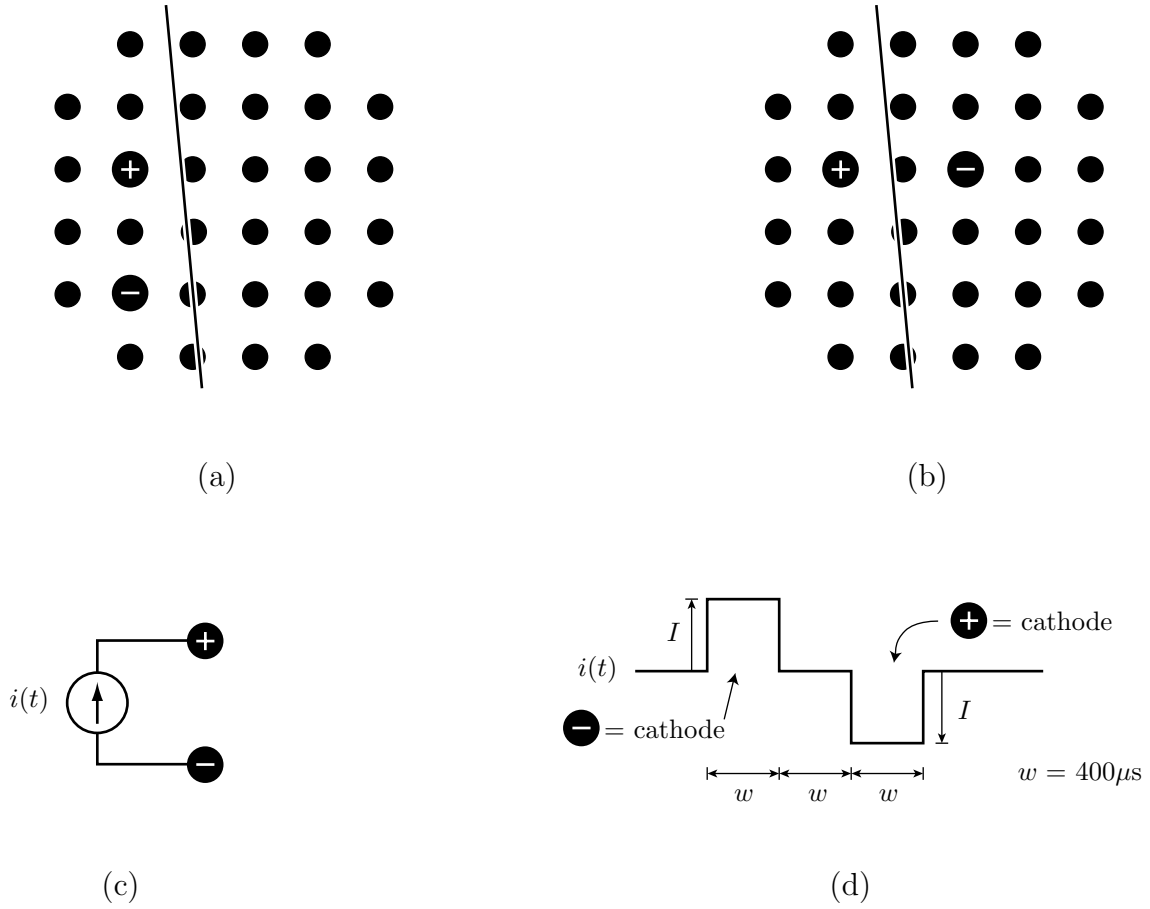

Figure 3.3: Bipolar stimulation: (a) Stimulation along the fiber; (b) Stimulation across the fiber; (c) Current source connections; (d) Drive waveform. Note that because the drive is biphasic, both the + and - electrodes are driven negatively (i.e. cathodically) during each stimulus presentation. The fiber location, indicated by a dark line in (a) and (b), was estimated from the map in Figure 2.13 using the method described in Section 3.3.2.

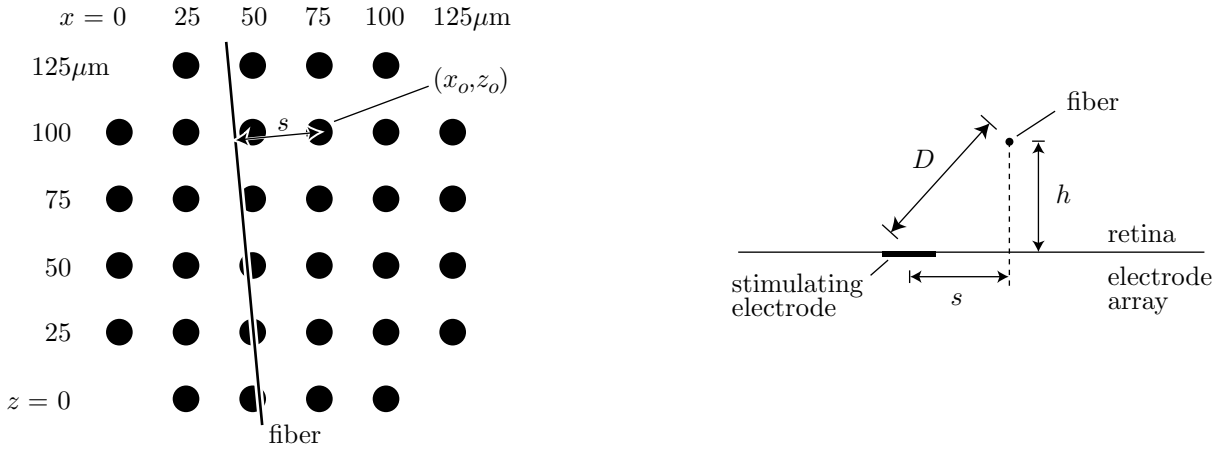

(a) (b)

Figure 3.4: Relative positions of electrodes and fiber. (a) Head on view of the array and fiber. s is the minimum distance from an electrode centered at (x_o, z_o) to the fiber's projection onto the plane of the array. (b) Cross-section view. The fiber extends out of the page, at a height h above the array.

separations. For reasons described in Section 3.4.2, the fixed and moving electrodes were chosen so that the fixed electrode had the lowest monopolar threshold of the three. One to five pairs of measurements was made on each of five fibers. The bipolar electrode pair separation d was always 50μm.

3.3.2 Data analysis

To use the models presented in Section 3.2 to estimate fiber positions, coordinate axes were superimposed on the fiber and stimulating electrodes, as shown in Figure 3.4(a). The fiber was assumed to be a straight line satisfying

$$\left.\begin{array}{c} x + bz + c = 0, \\ y = h, \end{array}\right\} \tag{3.8}$$

where b and c were unknown constants describing the position and angle of the fiber in the plane of the electrode array, and h was the unknown height of the fiber above the array. Defining s as the minimum distance from a point (x_o, z_o) in the xz-plane to the fiber's projection onto the plane, it followed that

$$s = \frac{|x_o + bz_o + c|}{\sqrt{1 + b^2}}, \tag{3.9}$$

$$D^2 = s^2 + h^2. \tag{3.10}$$

The relationship between D, s, and h is illustrated in Figure 3.4b.

The remaining steps in the position estimates differed slightly for the two models. The first principles model is used here to demonstrate the technique. The similar procedure for the empirical model is given in Section 3.6.

Substituting for D and s in equation 3.2 yielded

$$I_{thr} = k\left\{\frac{(x_o + bz_o + c)^2}{1+b^2} + h^2\right\}^{3/2} \tag{3.11}$$

Each threshold map consisted of a set of x_o's, z_o's, and corresponding I_{thr}'s from which the unknown parameters b, c, k and h could be estimated. This process began by re-writing equation 3.11

$$I_{thr}^{2/3} = a_1 x_o^2 + a_2 x_o + a_3 + a_4 x_o z_o + \left(\frac{1}{2}\frac{a_2 a_4}{a_1}\right) z_o + \left(\frac{1}{4}\frac{a_4^2}{a_1}\right) z_o^2, \tag{3.12}$$

where

$$a_1 = \frac{k^{2/3}}{1+b^2}, \tag{3.13}$$

$$a_2 = \left(\frac{k^{2/3}}{1+b^2}\right)(2c), \tag{3.14}$$

$$a_3 = k^{2/3}\left(\frac{c^2}{1+b^2} + h^2\right), \tag{3.15}$$

$$a_4 = \left(\frac{k^{2/3}}{1+b^2}\right)(2b). \tag{3.16}$$

A nonlinear least-squares fit was then performed on the two-thirds power of the thresholds to obtain parameters a_1, a_2, a_3, and a_4 which best satisfied equation 3.12 for each threshold map.

The parameters b, c, k and h were then calculated as follows:

$$b = \frac{a_4}{2a_1}, \tag{3.17}$$

$$c = \frac{a_2}{2a_1}, \tag{3.18}$$

$$k = \left[a_1(1+b^2)\right]^{3/2}, \tag{3.19}$$

$$h = \sqrt{\frac{a_3}{k^{2/3}} - \frac{c^2}{1+b^2}}. \tag{3.20}$$

The location estimate for the empirical model differed significantly from the preceding developments in that h could not be estimated independently from I_{min}. As discussed

in Section 3.6, an upper bound estimate for h, defined as h_{max}, was made by setting I_{min} to zero.

To plot thresholds versus distance, the displacement s on the retinal surface was calculated for each electrode by substituting b and c (estimated for each fiber) and x_o and z_o (defined for each electrode) into equation 3.9. The total displacement D could also be calculated from s and the estimated h, according to equation 3.10. Estimates for h were more strongly dependent on the choice of model than b and c, however (see Section 3.5.3), so s was used instead of D.

3.4 Results

3.4.1 Monopolar threshold vs. distance

Monopolar threshold maps were made for nine fibers in seven retinas. Individual threshold vs. displacement plots for the nine fibers, with best-fit curves for each, are shown in Figure 3.5 for the first principles model, and in Figure 3.6 for the empirical model.

The curves in Figures 3.5 and 3.6 were obtained by computing I_{thr} from equations 3.12 and 3.22, respectively, using the best-fit parameters a_1–a_4 for each fiber, at points (x_o, z_o) along a line perpendicular to the fiber. Error terms, also shown in each of the nine plots in each Figure, were obtained from

$$e = \sqrt{\frac{\Sigma_{i=1}^{N} \left(y_i - y_p(s_i)\right)^2}{N}}$$

where e is the error, N is the number of thresholds measured, y_i is the ith threshold measurement, s_i is the inferred distance on the retinal surface between the ith electrode and the fiber, and $y_p(s_i)$ is the theoretical prediction for the threshold at a displacement s_i.

Table 3.1 summarizes the results from the fiber position estimates using the first principles model. The estimates exhibit a range of nonzero tilt angles. This is due to imperfect alignment of retina patches on the array. Hence the bipolar measurements were approximately but not strictly parallel and perpendicular to the fibers. The range of x-intercept values simply indicates that fibers were studied at various horizontal displacements on the array. The h and k estimates and the error e will be considered in Section 3.5.3. Table 3.2 summarizes the same data for the empirical model.

The differences in tilt angles, x-intercepts, heights, and errors obtained with the two models are summarized in Table 3.3. The differences in tilt angles and x-intercepts are quite small when compared with the range of tilt angles observed and with the spacing between bipolar stimulating electrode pairs. The estimated heights of the fibers above the array were always higher for the first principles model than for the

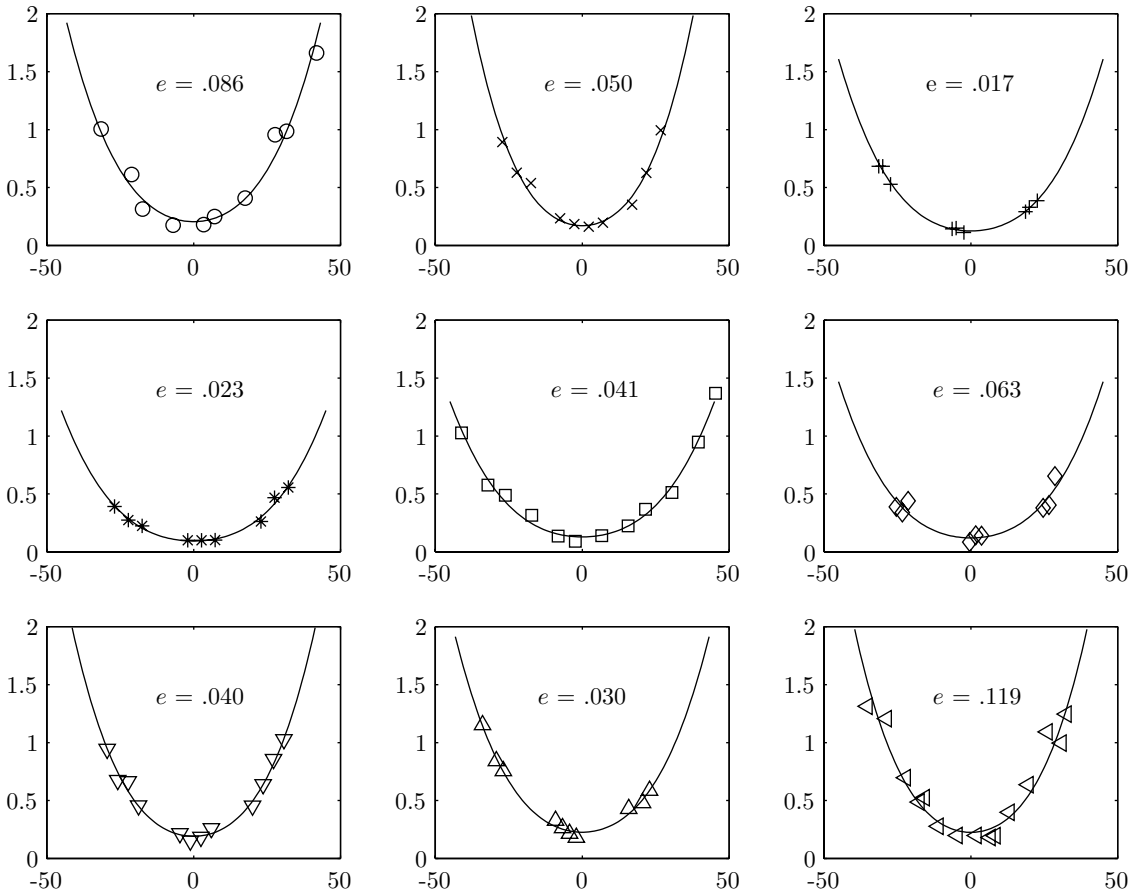

Figure 3.5: Measured data (symbols) and best-fit theoretical curves (first principles model) for monopolar threshold (vertical axes, in μA) vs. inferred displacement (horizontal axes, in μm) on the retinal surface, for each of nine fibers. Displacements were inferred using the first principles model. Negative displacements indicate stimulation on the left side of the fiber; positive displacements indicate stimulation on the right side of the fiber. An error term e, described in the text, is also given for each curve fit.

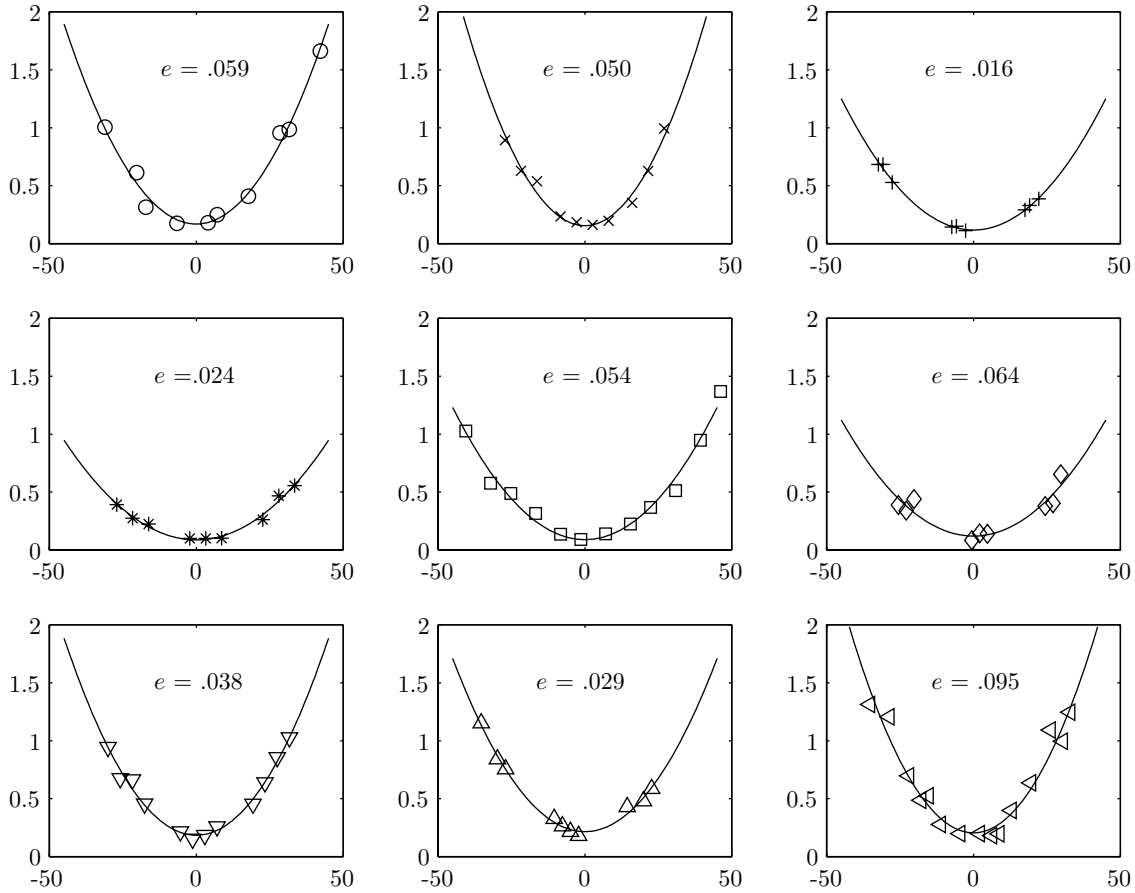

Figure 3.6: Measured data (symbols) and best-fit theoretical curves (solid lines) for monopolar threshold (vertical axes, in μA) vs. inferred displacement (horizontal axes, in μm) on the retinal surface, for each of nine fibers. Displacements were inferred using the empirical model. Negative displacements indicate stimulation on the left side of the fiber; positive displacements indicate stimulation on the right side of the fiber. An error term e, described in the text, is also given for each curve fit.

	Mean	Range
Tilt Angle	-5.2°	-17.3° to 8.2°
x-intercept	47.4μm	15.3 to 101μm
h	21.9μm	18.6 to 24.3μm
k	$1.6\times10^4\mu$A/mm^3	1 to $2.7\times10^4\mu$A/mm^3
e	.052μA	.017 to .119μA

Table 3.1: Curve fit statistics for fiber position estimates using the first principles model. The tilt angle was found by taking the inverse tangent of $-b$, and measures the fiber's angular deviation from vertical. The x-intercept, $-c$, indicates the horizontal displacement of the fibers along the top row of the stimulating grid.

	Mean	Range
Tilt Angle	-5.3°	-17.9° to 9.5°
x-intercept	47.5μm	13.7 to 101μm
h_{max}	14.4μm	12.1 to 17.1μm
$\hat{k}$	724μA/mm^2	424 to 1055μA/mm^2
e	.048μA	.016 to .095μA

Table 3.2: Curve fit statistics for fiber position estimates using the empirical model.

	Mean	Range
ΔTilt Angle	.2°	-1.3° to 1.3°
Δx-intercept	-.1μm	-1.4 to 1.6μm
Δh	7.5μm	6.1 to 10.9μm
Δe	.004μA	-.013 to .027μA

Table 3.3: Comparison of curve fit parameters for the first principles and empirical models. The table entries each represent a mean or range of nine Δs (one per fiber) each of which was computed by subtracting the empirical model estimate from the first principles estimate.

empirical model. The mean height difference was a substantial fraction of the mean height predicted by either model. This fraction was about 30% for the first principles model and about 50% for the empirical model. The goodness of fit is marginally better for the empirical model, as indicated by the small, positive Δe. A meaningful comparison cannot be made between the current-distance constants k and $\hat{k}$, since these have different units.

Figure 3.7 shows a summary plot of thresholds vs. s, the estimated electrode displacement on the retinal surface, for all nine fibers. Thresholds ranged from .1 to .2μA nearest the fiber and rose with displacement. Displacements were estimated in the Figure using the first principles model. The comparable plot for the empirical model (not shown) is nearly identical due to the close agreement in tilt angles and x-intercepts for the two models (Table 3.3).

3.4.2 Bipolar threshold vs. orientation

Bipolar thresholds were measured for five fibers in five retinas. Figures 3.8 and 3.9 plot the thresholds for stimulation along and across fibers as a function of the surface distance s from the fixed electrode to the fiber, where s was estimated using the first principles model and empirical model, respectively. Each symbol in these plots represents the ratio of a bipolar threshold to the monopolar threshold measured on the corresponding fixed electrode. The data in the two plots exhibit the same general trends. The along threshold ratios do not vary significantly with displacement, remaining close to one. The across threshold ratios, on the other hand, are close to one when the fiber is near the fixed electrode and rise rapidly for fibers at increasing proximity to the midpoint between the two poles ($s = 25\mu$m).

Theoretical predictions for the threshold ratios are also shown in Figures 3.8 and 3.9. These predictions were generated by extending the models for monopolar stimulation to the bipolar case, as described in Section 3.2.1 for the first principles

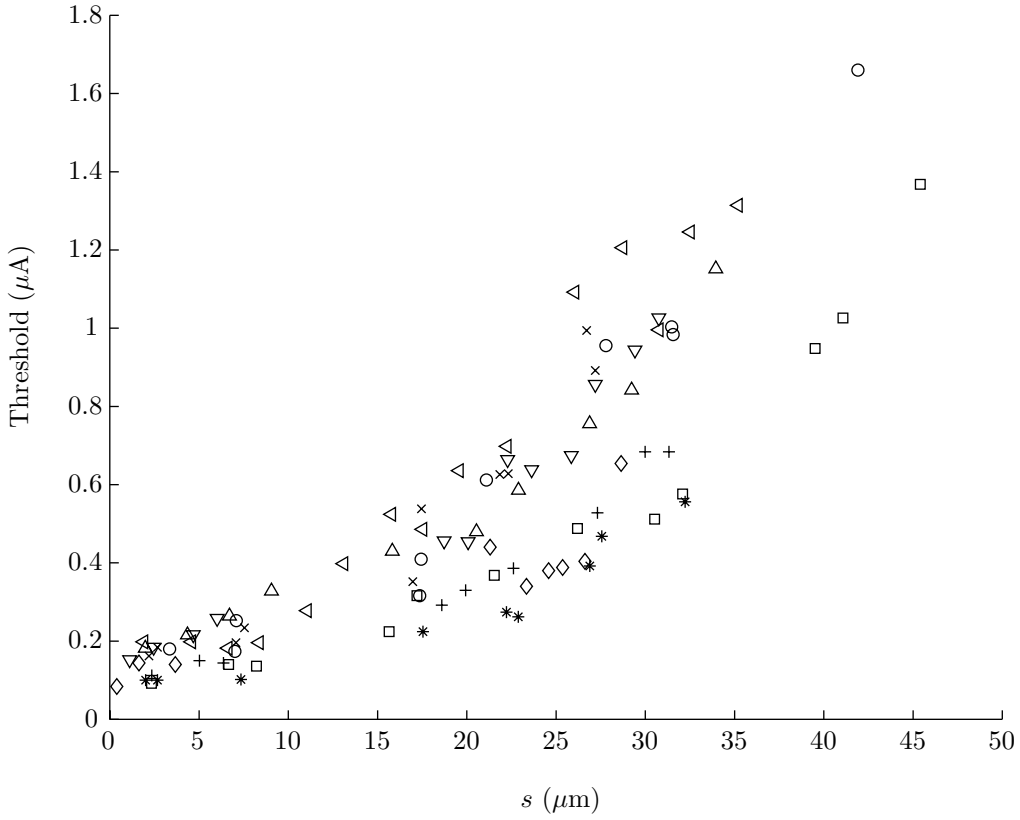

Figure 3.7: Monopolar threshold vs. inferred displacement s on the retinal surface (estimated using first principles model). Data from each cell is plotted with a unique symbol.

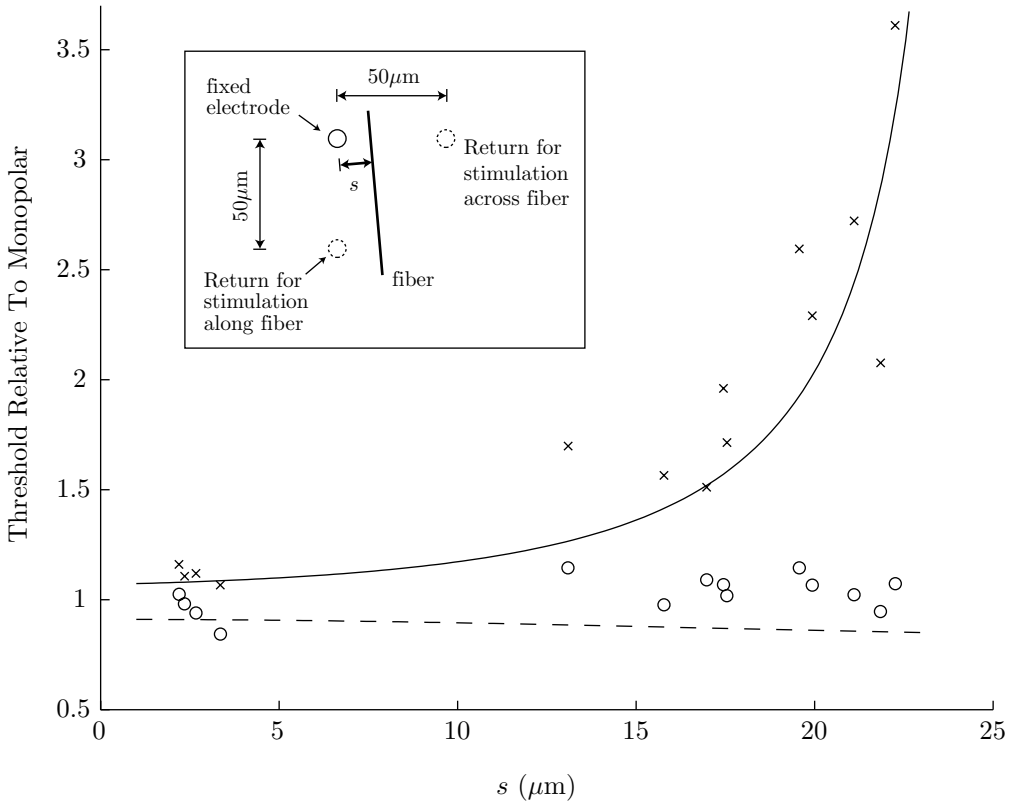

Figure 3.8: Normalized bipolar thresholds vs. inferred displacement s on the retinal surface (estimated using the first principles model), with theoretical curves superimposed. A $\times$ is used for thresholds measured with the bipolar electrode pair oriented across the fiber, and a $\circ$ when the pair was oriented along the fiber. Normalization was carried out by dividing each bipolar threshold by the monopolar threshold measured on the fixed electrode. Threshold predictions for stimulation along fibers are indicated with a dashed line, and predictions for stimulation across fibers are indicated with a solid line.

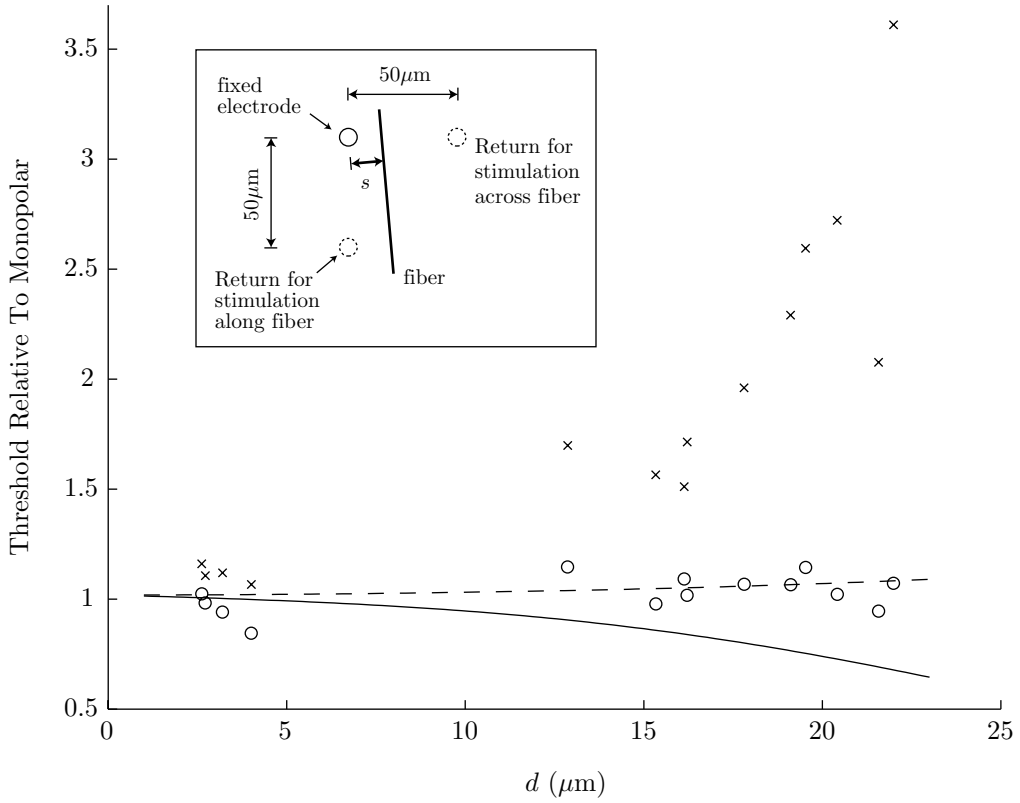

Figure 3.9: Normalized bipolar thresholds vs. inferred displacement s on the retinal surface (estimated using the empirical model), with theoretical curves superimposed. A $\times$ is used for thresholds measured with the bipolar electrode pair oriented across the fiber, and a $\circ$ when the pair was oriented along the fiber. Normalization was carried out by dividing each bipolar threshold to the monopolar threshold measured on the fixed electrode. Threshold predictions for stimulation along fibers are indicated with a dashed line, and predictions for stimulation across fibers are indicated with a solid line.

model and in Section 3.2.2 for the empirical model. The curves for stimulation along (dashed line) and across (solid line) fibers were produced by normalizing the bipolar threshold predictions for each model to its corresponding monopolar threshold prediction, assuming $h = 21.9\mu$m for the first principles model and $h = 14.4\mu$m for the empirical model (i.e. the mean values from the location estimates, given in Tables 3.1 and 3.2), and identifying $x_o = s$ and $d = 50\mu$m. While both models reasonably predicted thresholds for stimulation along fibers, only the first principles model provided a good prediction for stimulation across fibers.

The fixed electrode served as a general reference for the threshold comparisons in Figures 3.8 and 3.9: its position was used to determine the displacement s, and its monopolar threshold was used to normalize the bipolar thresholds. As described in Section 3.3.1, the fixed electrode was chosen so that it always had the lowest monopolar threshold of the three electrodes used to make the paired along/across measurements (see inset of Figure 3.8 or 3.9). This lowest-threshold electrode was used as a reference because it played the dominant role in excitation when used with a second, more distant electrode for bipolar stimulation. This dominance was indicated by a few experiments in which the sequence of anodal and cathodal pulses was reversed by either inverting the stimulation waveform or reversing the stimulator connections. In all cases, spike responses to threshold-level stimuli tracked the stimulus phase which drove the fixed electrode cathodically. Since cathodic thresholds are lower than anodic thresholds for monopolar stimuli (see Section 2.5.2), this behavior is consistent with localized excitation near the fixed electrode.

The preceding developments motivated the choice of stimulus sequence in Figure 3.3d. While thresholds were identical for both stimulus sequences, better separation of the responses from artifacts was achieved by driving the fixed (+) electrode cathodically for the second phase. Since the cathodic phase was responsible for excitation, this sequence ensured that responses were almost always recorded after the end of the stimulus. There were a few cases were suprathreshold stimuli evoked spikes which randomly followed either the first and second phase of the stimulus. In these cases the fiber was at very nearly the same distance from both poles of the bipolar pair (e.g. the fiber was near $s = 25\mu$m for across stimulation). Hence neither electrode played a dominant role. All spikes generated under such circumstances were counted—regardless of which stimulus phase they followed—when determining the threshold.

3.5 Discussion

3.5.1 Monopolar stimulation

Threshold order of magnitude

At points closest to the fibers, monopolar excitation thresholds ranged from approximately .1 to .2μA for a 400μs stimulus phase duration. Table 3.4 compares this result with thresholds reported by others who placed stimulating electrodes against the epi-retinal surface.

The reported threshold currents span a range of over three orders of magnitude, with the threshold currents in this study falling about a factor of five below the lowest threshold reported previously. Some of the variability can be accounted for by differences in stimulation parameters. Threshold currents are modestly correlated with electrode area, for example. Electrode areas were less than 10^{-6}cm^2 in the three cases where threshold currents were below a microampere, and greater than 10^{-6}cm^2 for larger threshold currents. Expressing thresholds as average current densities (threshold $\div$ area)* reduces the variability by an order of magnitude. These results are not surprising since a simple electric field calculation shows that, near the surface of a spherical stimulating electrode, the current required to produce a given voltage gradient increases with electrode radius (Ranck, 1981)†. Since phase durations were not all the same, some of the variability in the current and current density thresholds might be accounted for by classic strength-duration behavior. In the three studies reporting sub-microampere threshold currents, for example, the total charge (current $\times$ phase duration) varied by less than a factor of two despite a five- to six-fold variation in threshold current. Expressing thresholds as an average charge density (charge $\div$ area)†, which takes into account both the phase duration and the electrode area, results in less variability than the currents but slightly larger variability than the current densities. The remaining variability might be accounted for by a number of methodological differences, including the electrode shape, the species studied, or the site of initial excitation within the retina.

Although the threshold currents reported in this study are quite low when compared with other retinal stimulation experiments, these were not unusually low when expressed as average current densities and average charge densities. Furthermore, comparably low current thresholds for extracellular stimulation have appeared in

*Note that the average current and charge densities may not represent the actual distribution of current and charge in real electrodes, since stimulating electric fields are not necessarily uniform across electrode surfaces In addition, some caution is in order when using current and charge densities, since both will tend to rise without limit as the electrode area approaches zero, and the charge density will rise without limit for stimulus phase durations well above chronaxie.

†Ranck calculated the current needed to cause a 30mV difference in voltage between a site just adjacent to the electrode and another site 600μm away. For electrode radii between 1μm and 100μm, this current appeared to scale with electrode radius. In the limit where the radius becomes very large compared to 600μm, the requisite current is proportional to the square of the radius.

Study	Threshold current	Electrode area	Current density	Phase duration	Phase charge	Charge density
Dawson & Radtke (1977)	65μA	4.91×10^{-6} to 7.90×10^{-4}cm^2		800μs		30.5μC/cm^2
Greenberg (1998c)	206μA	1.26×10^{-3}cm^2	163mA/cm^2	520μs	1.07×10^{-7}C	85μC/cm^2
Humayun et al. (1994)	50μA (frog)	1.26×10^{-3}cm^2	40mA/cm^2	75μs	3.75×10^{-9}C	2.98μC/cm^2
	150μA (rabbit)	1.26×10^{-3}cm^2	119mA/cm^2	75μs	11.2×10^{-9}C	8.92μC/cm^2
	200μA (rd rabbit)	1.26×10^{-3}cm^2	159mA/cm^2	75μs	15×10^{-9}C	11.9μC/cm^2
Humayun et al. (1999)	(phosphenes)	1.26×10^{-3}cm^2 (array)		$\leq$2ms	5×10^{-7}C	397μC/cm^2
Jensen et al. (1996)	8μA	7.8×10^{-5}cm^2 (bipolar)	102mA/cm^2	200μs	1.6×10^{-9}C	20μC/cm^2
(near soma)	.8μA	1.6×10^{-7}cm^2 (monopolar)	5000mA/cm^2	100μs	8×10^{-11}C	500μC/cm^2
Rizzo et al. (1997)	16μA	7.8×10^{-5}cm^2 (bipolar)	205mA/cm^2	200μs	3.2×10^{-9}C	41μC/cm^2
(axon)	.9μA	1.6×10^{-7}cm^2 (monopolar)	5625mA/cm^2	100μs	9×10^{-11}C	562μC/cm^2
This study	.15μA	7.8×10^{-7}cm^2	192mA/cm^2	400μs	6×10^{-11}C	77μC/cm^2

Table 3.4: Summary of thresholds for stimulation at the epi-retinal surface. Entries were left blank where relevant information could not be determined. For studies where a range of thresholds was reported rather than a mean or median, the table entries represent the average of the minimum and maximum values reported. For studies where thresholds were reported at various positions of the stimulating electrode, the table data represent measurements at the lowest-threshold position. And for studies where both anodal and cathodal monopolar stimuli were used, the table data represent cathodal thresholds only. Doty & Grimm (1962) also placed stimulating electrodes the epi-retinal surface (see Table 1.1), but reported thresholds in terms of voltage rather than current and did not report the electrode area. *Abbreviations:* rd = retinal degenerate (experimentally induced).

previous studies of other neural systems (Ranck, 1975).

Spatial extent of stimulation

The spatial extent of fiber excitation for a given stimulus amplitude may be estimated from the plot of Figure 3.7 by superimposing a horizontal line at the desired level and finding its intercept with the data. A .2μA stimulus, for example, would be expected to excite fibers within about 10μm of the of the stimulating electrode since thresholds were higher at larger distances. Similarly, a 1μA stimulus will excite fibers within 40μm of the electrode. Such estimates are somewhat simplistic, however, because they fail to take into account the fact that cathodal pulses far above threshold can fail to generate propagated action potentials (Ranck, 1975). This effect is caused by hyperpolarization in regions where stimulation currents enter the fiber, away from the cathode. Hence for sufficiently large cathodal currents there will be a central region of non-stimulated fibers surrounded by an annular, stimulated region. No attempts were made in the present study to detect or characterize this phenomenon.

The rise of thresholds with electrode displacement away from the target has been studied elsewhere. Rizzo et al. (1997) measured axon excitation thresholds vs. stimulating electrode position in rabbit retina using three different stimulation protocols. For the protocol most resembling the present experiments (Protocol II), median thresholds rose by a factor of six when the electrode was displaced to $s = 50\mu$m[‡]. Greenberg (1998c) measured excitation thresholds for ganglion cells in frog retina, and found that displacements of several hundred microns were required for a 1.4-fold (i.e. 3dB) increase in threshold. Stimulation in the present study was somewhat more focal than in the previous two cases, since thresholds rose by roughly a factor of ten at a distance of 40μm. The current-distance constants k and $\hat{k}$ in Tables 3.1 and 3.2 also measure the spatial extent of stimulation. The range of values listed for $\hat{k}$ is similar to those found in other neural systems (Tehovnik, 1996).

3.5.2 Orientation dependence

Figures 3.8 and 3.9 show that fiber excitation thresholds were sensitive to the orientation of the stimulating electric field. Thresholds for each fiber were highest when the stimulating field was most nearly perpendicular to its long axis, achieved in practice when the fiber was most nearly at the midpoint between the two poles used for transverse bipolar stimulation. When the fiber was within 5μm of this midpoint, thresholds were about a factor of 2 to 3.5 larger than when monopolar or longitudinal bipolar stimulation was used.

Note, however, that even in these cases the estimated fiber paths were still 2-3μm away from the midpoint between the two poles and were often tilted with respect to

[‡]Rizzo et al. used the variable name y, rather than s, to measure distances along a line perpendicular to the axon's course.

vertical. The first principles model predicts that thresholds will become infinite as the fiber approaches this midpoint, but this is simply a consequence of one of the model's assumptions. The model assumes, as do many in the extracellular stimulation literature, that the transverse component of the stimulating field contributes negligibly to excitation (McNeal, 1976; Rattay, 1986; Rubinstein and Spelman, 1988; Warman et al., 1992). The assumption arises from the common occurrence of both transverse and longitudinal field components in the experimental literature. The transverse voltage drop across a fiber's outer surface is usually small, at least when compared to the voltage drop developed by the longitudinal component of the field, owing to the fiber's small diameter.

Such justification would not apply if the stimulating field were purely transverse. Suppose for the sake of argument that purely transverse fields were insufficient to produce excitation in fibers. In practice, one would still not expect thresholds with optimally positioned electrodes to become unbounded for at least two reasons. First, electrical inhomogeneities or anisotropies in the tissue could deflect the stimulating field to generate longitudinal field components. Second, at high enough currents other regions of the same cell or pre-synaptic elements will be stimulated. On the other hand, the most dramatic increases in threshold are expected to occur within the vary narrow, as yet unexplored gap of $\approx 3\mu$m between the best-centered data points in Figure 3.8 and the exact center at 25μm. It therefore seems reasonable that a more exhaustive study could reveal larger threshold ratios in a narrow band at the center of the bipolar electrode pair.

3.5.3 Models

Monopolar stimulation and location estimates

Both the first principles and empirical models provided provided a good fit to the data. The goodness of fit, as measured by the error term e, was similar for the two models. The mean error was marginally larger for the first principles model than for the empirical model (see Tables 3.1 and 3.2). In both cases, this mean error was at least a factor of two smaller than the lowest thresholds observed. The best-fit curves for the two models were nearly identical, as could be verified by overlaying the plots in Figures 3.5 and 3.6. The largest differences were seen near $\pm 50\mu$m, where the curves for the first principles model sometimes rose more steeply than those for the empirical model. A more competitive comparison of the two models would likely be possible if threshold data were available for a larger range of electrode displacements.

The two models differed significantly in their estimates for the fibers' heights h above the array (Table 3.3). On average, the upper bound height h_{max} predicted by the empirical model was 7.5μm less than the height predicted by the first principles model. This discrepancy is simply a consequence of the difference in steepness of the threshold vs. electrode-fiber distance curves in the two models. The steeper first principles model predicts a larger height because this results in a slower increase of

total distance—and hence a slower increase of predicted thresholds—with increasing surface distance (the independent variable in the monopolar threshold maps).

Estimates for the fibers' projections onto the electrode array plane, described by the tilt angle and $x-$intercept (or equivalently by b and c), were more certain. The two models provided nearly identical estimates for these projections. Furthermore, whole-mount stains from other studies (Peichl et al., 1987; Vaney, 1980) show that in small regions away from somata such as that spanned by the stimulating cluster in Figure 2.2, it is very reasonable to assume that axons follow straight-line paths. A possible weakness in the model is the assumption that fibers run at a constant height above the array. Hence errors could be introduced into the tilt angle and x-intercept estimates if threshold variations across the maps were partially due to height variations. This possibility was explored by assigning an out-of-plane slope r to the fiber such that

$$h = h_o + rz$$

and re-estimating the parameters b, c, h_o, and k using the first principles model. For an r-range corresponding to an out-of-plane slope of -5° to 5° (or a height difference of over 10μm across the 125μm span of the array), the in-plane tilt angle varied by no more than 3.3° and the x-intercept varied by less than 2μm[§]. Hence the location estimates were not substantially changed when height of the fiber was allowed to vary. Because the actual height of the fibers above the array was uncertain, the surface displacement s was used in the threshold plots rather than the total displacement D.

The accuracy of the fiber position estimates might be improved by imaging retinas during experiments. This approach was not attempted in the present study, primarily because optical access was impeded from above by the dialysis membrane holding the patch in place, and below by the opaque chrome/gold electrode conductors. The latter problem can be remedied by using indium tin oxide (Meister et al., 1994), a transparent conductor, instead of chrome/gold. The large number and complex arrangement of neural elements could also make it difficult to correctly identify the precise fiber under study. Conducting studies in peripheral retina should increase the chances of uniquely identifying the axon under study.

Bipolar thresholds

While both models reasonably predicted thresholds for stimulation along fibers, only the first principles model provided a good prediction for stimulation across fibers (Figures 3.8 and 3.9). Predicted thresholds fell with increasing s in the empirical model because the maximum field magnitude *was larger* between the two poles of transverse bipolar pair than at a comparable distance from a monopolar electrode, even though the longitudinal component of the field was reduced. Since the physi-

[§]At larger out-of-plane slopes, the software routine used for least-squares estimation—MATLAB's `nlinfit` function—either converged to non-real (i.e. complex) values or did not converge at all.

ologic thresholds rose for transverse bipolar stimulation, electric field strength alone does not accurately predict fiber excitation thresholds.

Use of the activating function

The first principles model made a number of assumptions in order to permit a purely theoretical formulation. For example, the activating function rather than the membrane potential was used to gauge thresholds. Because it ignores the distribution of stimulating currents in the fiber, the activating function only approximates the membrane potential profile generated by a stimulus (Warman et al., 1992). The main advantage of this approach is that it eliminated the need to model membrane electrical properties, which are nonlinear and would have required computer simulation.

3.5.4 Axons or dendrites?

The possibility was raised in Chapter 2 that some or all of the recorded responses might be due to stimulation of dendrites rather than axons. Hence the use of the more general term *fiber*. Since both axons and dendrites share the same basic cylindrical geometry, the identity of the target little effects the primary result of this Chapter. However, it seems reasonable to suggest that responses were due at least in part, if not in total, to stimulation of axons. The dendrites stratify in the inner plexiform layer, several tens of microns further than axons from the stimulating electrode plane. The very lowest excitation thresholds would therefore be expected for axon excitation. Furthermore, the magnitude of current necessary for stimulating axons could be judged from the minimum amplitude which produced graded potentials. These magnitudes were not systematically lower than the spike thresholds, as would be expected if spikes arose only as a result of dendrite stimulation.

The height estimates yielded by the first principles and empirical models are consistent with stimulation of elements near the retinal surface, but do not conclusively identify the stimulation target. The empirical model yielded an upper bound h_{max} on the fiber height of 17.1μm or less. Assuming that the arrays were in direct contact with the inner limiting membrane (ILM), this range of heights could be consistent with with either axon or dendrite stimulation. The first principles model yielded height estimates of 18.6μm or more. For arrays in direct contact with the ILM, this range of heights would not be consistent with axon stimulation because the nerve fiber layer is only about 10μm thick in the retinal regions where these studies were conducted. On the other hand, it is likely that the model over-estimated the heights, since at the same current a 10μm diameter electrode would have to be closer to its target than a point source in order to generate an equally strong activating function. It is also possible that the electrode arrays were not in direct contact with the ILM, but separated from it by a thin layer of vitreous. Hence the height estimates from the first principles model do not rule out axon stimulation.

A more definitive statement about the stimulation target could be made if the stimulating and recording clusters were placed further apart than the largest dendritic spreads, perhaps 1mm or more. In the present experiments the cluster separation was kept small to reduce the sensitivity of the measurement to imperfect vertical alignment of axons. At larger separations, the chances of recording from a cell whose axon ran through the stimulating cluster would be reduced.

3.6 Appendix: Location estimates using the empirical model

Equation 3.5 was used to estimate fiber locations in a manner analogous to that described in Section 3.3.2. Threshold map data are incorporated into this model according to

$$I_{thr} = \hat{k}\left\{\frac{(x_o + bz_o + c)^2}{1+b^2} + h^2\right\} + I_{min}. \tag{3.21}$$

(see Section 3.3.2 and Figure 3.4 for descriptions of the variable definitions).

The parameters b, c, and $\hat{k}$ were estimated by re-writing this relation as

$$I_{thr} = a_1 x_o^2 + a_2 x_o + a_3 + a_4 x_o z_o + \left(\frac{1}{2}\frac{a_2 a_4}{a_1}\right) z_o + \left(\frac{1}{4}\frac{a_4^2}{a_1}\right) z_o^2, \tag{3.22}$$

where

$$a_1 = \frac{\hat{k}}{1+b^2}, \tag{3.23}$$

$$a_2 = \left(\frac{\hat{k}}{1+b^2}\right)(2c), \tag{3.24}$$

$$a_3 = \hat{k}\left(\frac{c^2}{1+b^2} + h^2\right) + I_{min}, \tag{3.25}$$

$$a_4 = \left(\frac{\hat{k}}{1+b^2}\right)(2b). \tag{3.26}$$

Performing a nonlinear least-squares fit yields parameters a_1, a_2, a_3, and a_4 which best satisfied equation 3.22 for each threshold map.

Estimates for each cell's b, c and $\hat{k}$ were then calculated as follows:

$$b = \frac{a_4}{2a_1}, \tag{3.27}$$

$$c = \frac{a_2}{2a_1}, \tag{3.28}$$

$$\hat{k} = a_1(1+b^2). \tag{3.29}$$

The parameters h and I_{min} could not be estimated independently because these contributed only additive terms to the threshold maps. However, a maximum bound on h could be estimated by assuming $I_{min} = 0$. The upper bound, h_{max}, was given by

$$h_{max} = \sqrt{\frac{a_3}{\hat{k}} - \frac{c^2}{1 + b^2}}.$$

Chapter 4

Conclusions

4.1 Strengths and weaknesses of new experimental method

A significant proportion of the effort in this thesis was aimed at the development of new techniques for characterization of retinal responses to electric stimulation. It is useful at this point to consider the advantages and disadvantages of these techniques.

4.1.1 Stimulating electrode arrays

The main strength of the new experimental setup was its use of microfabricated stimulating electrode arrays. With these arrays it was a simple matter to quickly perform a number of threshold measurements with a number of electrode configurations, all without any mechanical disruption of the retina preparation. Furthermore, arrays provide the experimenter with detailed control over the shape and distribution of electrodes. Though in this study conventional disk shapes of a uniform size were used, future work is likely to benefit from more complex and unconventional electrode arrays (see Chapter 5).

A possible drawback of the stimulating array approach is that unused electrodes on the array can play a role in shaping the stimulating electric field distribution*. The exposed metal electrode surfaces are equipotentials in the frequency ranges of interest to electrophysiologic studies, and will tend to equalize tissue potentials in their immediate vicinity. The extent of field distortion from unused electrodes will depend on the relative sizes of the tissue impedance and electrode interface impedances. Such distortion needs to be taken into account in particular when considering experiments with large, closely-spaced electrodes, as discussed in Section 5.4.

*This was first pointed out to me by a member of my thesis committee, Don Eddington.

4.1.2 Recording arrays

Multi-electrode recording systems permit simultaneous monitoring of activity at many sites in a tissue. In the measurements described in Chapters 2 and 3, this capability was utilized to record correlated spontaneous firing, which in turn suggested the anatomical substrates underlying different spike waveforms (see Figure 2.6 and Section 2.6), and to speed up the search for sites within the recording cluster exhibiting single unit responses to electric stimulation. Multi-channel recordings were not employed for the mapping and orientation measurements, though in principle they could be. For such an approach it would be useful to have an automated system for determining excitation thresholds, which in turn would require a means of discriminating all-or-none responses from graded responses and stimulus artifacts.

The main drawback of the new method is that each recording electrode tends to pick up multiple units. Hence the ubiquitous graded potentials, which required a tedious search for sites with clean all-or-none potentials for stimulation at a number of different stimulating electrode positions. With its smaller tip diameter and ability to penetrate the surface, a needle-shaped recording electrode provides better isolation of single units. On the other hand, this geometry does not lend itself as easily to multi-electrode studies (but see Normann, 1999).

4.1.3 Soma stimulation

The setup did not lend itself well to measuring thresholds for excitation of somas and associated structures (i.e. the axon hillock and initial segment). Such experiments are most easily performed by applying stimuli in the vicinity of a ganglion cell's optic receptive field center and recording the orthodromic responses at a location along the cell's axon. In the present setup, axon spikes (Type 2 in Figure 2.6) were usually smaller and more difficult to discriminate than the soma spikes (Type 1). Early attempts were made to both stimulate and record from the soma by stimulating through electrodes which were very close to a recording electrode with Type 1 spikes, but stimulus artifacts always obscured at least the first 3-5ms of the response. While difficult for flat recording electrodes, soma threshold measurements can be more readily made with needle-shaped recording electrodes which better isolate single axons.

4.2 Related work re-considered

Chapter 3 demonstrated that thresholds for retinal ganglion cell axons (and possibly dendrites) depended in a consistent manner on the orientation of a bipolar stimulating electrode. Thresholds were highest when the imposed electric field was most nearly perpendicular to fibers, achieved in practice when the fiber was near the midpoint between the two poles of a transversely oriented bipolar electrode pair. This result

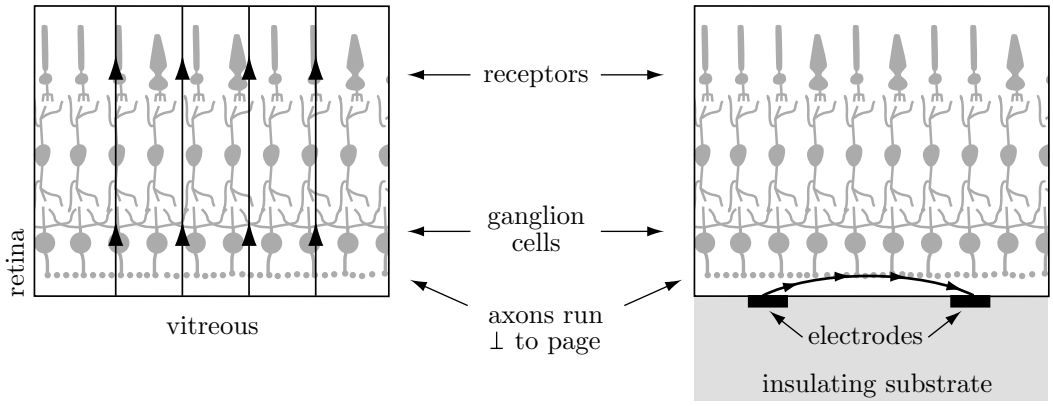

Figure 4.1: Both transretinal (left) and transverse bipolar (right) stimulation produce stimulating fields which run perpendicularly to axons.

is consistent with theoretical predictions (Plonsey and Altman, 1988; Grumet, 1994) and experimental work in other neural systems (Ranck, 1975; Rushton, 1927).

This result also indicates that axon thresholds will be comparatively high for transretinal current (Figure 4.1, left hand side). Like the current from a carefully placed transverse bipolar electrode pair (Figure 4.1, right hand side), transretinal current runs perpendicularly to ganglion cell axons. Furthermore, initial excitation of deeper elements such as photoreceptors and bipolar cells is perhaps more likely under these conditions (Greenberg, 1998a). Except in regions of high receptor density, a number of receptor and bipolar cells will converge on each ganglion cell. Because the ganglion cell can spatially integrate synaptic contributions to its membrane potential from many bipolar cells—each of which can integrate contributions from many photoreceptors—weak stimulation of a population of pre-synaptic cells could conceivably result in ganglion cell spiking at current levels below the threshold for direct ganglion cell stimulation.

In the majority of the studies listed in Table 1.1, stimulating electrodes were placed at a considerable distance (500μm or more) from the epi-retinal surface. It seems likely that in many such cases the fields were either stronger in other parts of the retina than at the epi-retinal surface, or were predominantly transretinal. In two studies, electrodes were placed outside the eye, against the sclera (Brindley, 1955; Greenberg, 1998a). Reponse characteristics in these studies were consistent with stimulation by the transretinal component of the field. If the stimulating fields were not purely transretinal, they would have been strongest in regions closer to the

electrode such as the photoreceptor or bipolar cell layers. In other studies, stimulation current was passed between a monopolar electrode in the vitreous and a distant, extra-ocular return (Crapper and Noell, 1963; Humayun et al., 1996; Humayun et al., 1999). The low resistivity of the vitreous relative to that of the retina, choroid and sclera (Ogden and Ito, 1971; Rodieck, 1973) probably reduced voltage gradients in the retinal plane—and hence, along axons—so that most of the field ran perpendicularly to the retina. These observations may account for the fact that axons were not maximally sensitive to electric stimulation in many of the studies in Table 1.1.

In a retinal prosthesis the stimulating electrodes must be placed at the retinal surface to keep the excitation thresholds as low as possible. Even when monopolar configurations were used, thresholds rose rapidly with distance as the stimulating electrode was raised above the epi-retinal surface (Humayun et al., 1999; Jensen et al., 1996). Electrodes placed against the epi-retinal surface will produce the largest voltage gradients in the adjacent nerve fiber layer. This effect will be especially pronounced when electrodes reside on a planar, insulating substrate since in this case shunt paths through the vitreous will not be available. Hence axons are particularly likely to be stimulated by the electrode configuration which will be used by a retinal prosthesis.

Stimulating electrodes were placed at the retinal surface in only four of the studies permitting threshold comparisons for axons and other elements (Doty and Grimm, 1962; Greenberg, 1998c; Humayun et al., 1999; Jensen et al., 1996), and were mounted on insulating backplanes in only two (Greenberg, 1998c; Humayun et al., 1999). The results were mixed, with axons sometimes maximally sensitive in two of the studies (Greenberg, 1998c; Jensen et al., 1996), but not maximally sensitive in the other two (Doty and Grimm, 1962; Humayun et al., 1999). Differences in stimulus phase duration may partially account for this variability (see Section 1.2.3), though the pulse duration hypothesis has not yet been tested with a realistic electrode configuration (see Section 5.3). As discussed in Chapter 5, further work needs to be conducted to determine whether axon stimulation can be avoided with electrodes resembling those which will be used in an eventual prosthesis.

4.3 Implications for epi-retinal prosthesis design

Thresholds only rose for transverse bipolar stimulation when fibers were nearly centered between the two poles of the bipolar pair. When the fiber was within 5μm of either electrode, thresholds for monopolar, longitudinal bipolar, and transverse bipolar stimulation were about equal. Hence in an epi-retinal prosthesis, transverse bipolar electrodes made of 10μm diameter disks would only raise axon thresholds within narrow bands between the electrodes in each bipolar pair. Furthermore, bipolar electrodes might actually stimulate fibers over a wider area of retina than monopolar electrodes, depending on the choice of stimulation current waveform. This possibility is explained in Figure 4.2.

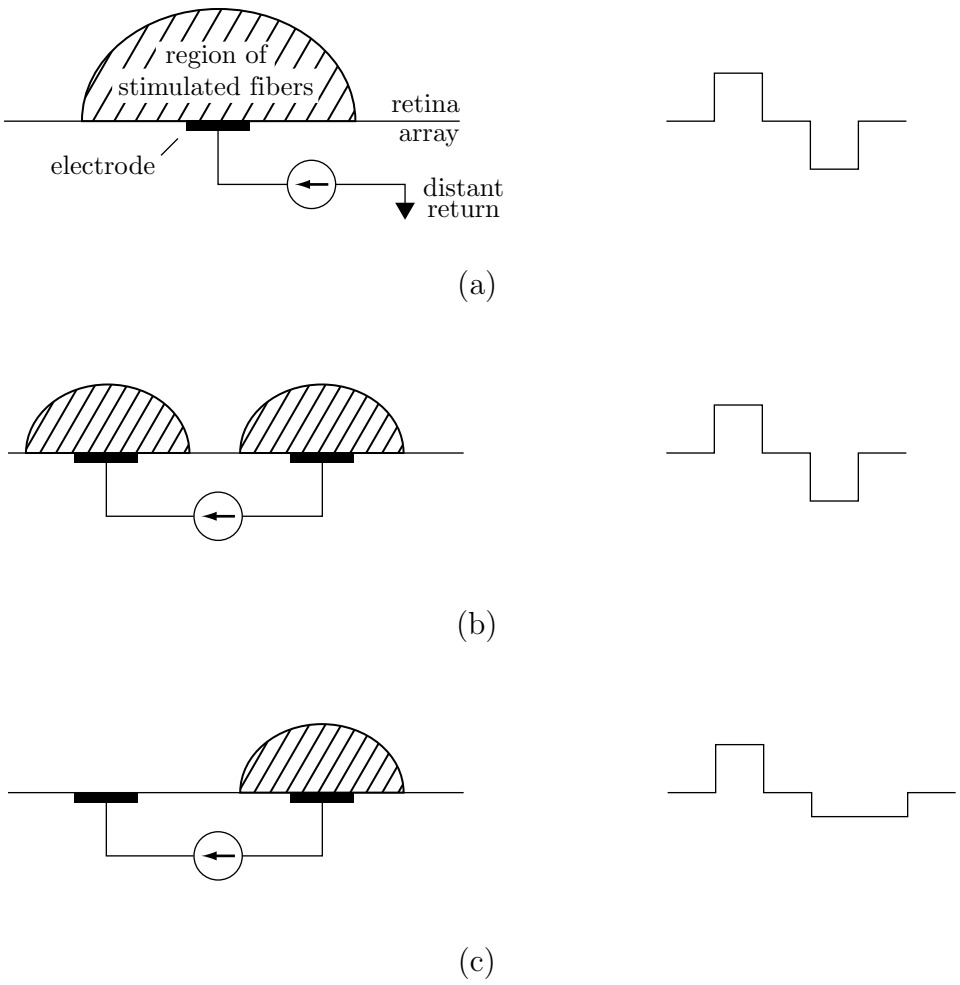

Figure 4.2: Highly schematic comparison of excitation patterns for monopolar and transverse bipolar stimulation. Left column: electrode configurations and extents of excitation; right column: stimulation current waveforms. (a) Stimulation with a monopolar electrode; (b) and (c) Stimulation with bipolar electrodes. For bipolar stimulation, the extent of excitation around each electrode will be less than for monopolar stimulation. However, for bipolar stimulation and sufficiently large stimuli, as in (b), excitation will be initiated over both poles of the bipolar pair during the corresponding cathodic phase. Excitation on one of the poles can be minimized by choosing an asymmetric stimulation waveform as in (c), provided that the waveform is charge-balanced and the longer pulse duration is well above chronaxie.

The findings in this thesis demonstrate that longitudinal fields are more efficient for stimulating axons than transverse fields. Minimizing axon stimulation therefore requires an electrode design which minimizes longitudinal field components between the poles of a bipolar electrode pair as well as in the immediate vicinity of each electrode.